The Radiated Field Generated by a Monopole Source in a Short, Rigid, Rectangular Duct

by

Barbara Anne Lakota

B. S. Mechanical Engineering May 1995, Western New England College

A Thesis submitted to

The Faculty of

The School of Engineering and Applied Science
of the George Washington University in partial satisfaction
of the requirements for the degree of Master of Science

March 13, 1998

Thesis directed by

Dr. M. K. Myers
Professor of Engineering and Applied Science

This research was conducted at NASA Langley Research Center

Abstract

This thesis develops a method to model the acoustic field generated by a monopole source placed in a moving rectangular duct. The walls of the duct are assumed to be infinitesimally thin and the source is placed at the center of the duct. The total acoustic pressure is written in terms of the free-space pressure, or incident pressure, and the scattered pressure. The scattered pressure is the augmentation to the incident pressure due to the presence of the duct. It satisfies a homogeneous wave equation and is discontinuous across the duct walls. Utilizing an integral representation of the scattered pressure, a set of singular boundary integral equations governing the unknown jump in scattered pressure is derived. This equation is solved by the method of collocation after representing the jump in pressure as a double series of shape functions. The solution obtained is then substituted back into the integral representation to determine the scattered pressure, and the total acoustic pressure at any point in the field. A few examples are included to illustrate the influence of various geometric and kinematic parameters on the radiated sound field.

Acknowledgments

The author would like to thank Dr. M.K. Myers for his time, knowledge and experience in successfully guiding the research presented in this thesis as well as Dr. F. Farassat and Mr. Robert Grandle for their generosity and expertise. The staff at the JIAFS/GWU office also need to be thanked for their willingness to assist with any problem. The author would also like to thank Jeff Parker and James Leary for their assistance.

Table of Contents

List of Symbols

A	Source strength
a	Duct dimension
$a_{j,k}$	Constant in shape function expansion for π
b	Duct dimension
B_o	$X_3^2/\beta^2+X_2^2+X_1^2$
B	$\xi^2 + h^2 + \eta^2$
c	Speed of sound of the undisturbed medium
D*	Offset distance from leading and trailing edges of duct
f	Functional description of the duct surface
F	Integrand of eqn. (2.30)
G	Integrand of eqn. (2.36)
i	$\sqrt{-1}$
$\left(I^{(\ )}\right)_{j,k}$	Contributions from sides (4)
$I_j^{(pv)}$	Cauchy principal value
I_S	Isolated singular term
J	Total number of shape functions in axial series
K_1	Total number of shape functions for surface $X_1 = \pm a$
K_2	Total number of shape functions for surface $X_2 = \pm b$
$K^{(\ )}$	Components of boundary integral equation

L	Length of duct
M	Forward Mach number
$\hat{n}$	Unit normal to duct surface
N_S	Number of panels in Y_1 or Y_2
N_κ	Number of panels in Y_3
p_i	Incident pressure
p_{ref}	Reference pressure, $2x10^{-5}$ Pa
p_{rms}	Root-mean squared average pressure
p_t	Total pressure
p_s	Scattered pressure
p	Complex pressure amplitude
Δp_s	Scattered pressure jump
P_λ	Panels per wavelength
q	Acoustic noise source
Q_S	Treated singular term
r	Magnitude of the radiation vector
$\bar{r}$	Radiation vector
SPL	Sound pressure level, decibels re p_{ref}
t	Observer time
V	Magnitude of forward velocity
$\bar{x}$	Observer position in inertially-fixed reference frame
$\bar{X}$	Observer position in body-fixed reference frame

$\bar{X}_s$	Surface observer coordinates (X_1,X_2,X_3)
$\bar{y}$	Source location in the inertially-fixed reference frame
$\bar{Y}$	Source location in the body-fixed reference frame
$\bar{Y}_s$	Surface source coordinates (Y_1,Y_2,Y_3)
α	$\omega/c\beta$
β	Compressibility factor, $\beta^2 = 1 - M^2$
κ	Axial source variable (eqn. 3.1)
$\delta(\cdot)$	Dirac delta function
$\pm\delta$	Limits on local integrals
$\varphi_j(Y_3)$	Axial shape functions
$\psi_k(Y_n)$, n=1,2	Lateral shape functions
λ_s	Wavelength for oscillations in Y_2
λ_κ	Wavelength for oscillations in κ
ω	Frequency
π_1	X_3, X_2 dependent scattered pressure jump amplitude function
π_2	X_3, X_1 dependent scattered pressure jump amplitude function
τ^*	Solution to retarded time equation
τ	Emission time
ρ_o	Density of undisturbed medium
θ	Angle between $\hat{n}$ and $\hat{r}$ or spherical observer angle for far field
ξ	$(Y_3 - X_3)/\beta$

η	Y_2-X_2
ζ	Y_1-X_1
ϕ_i	Velocity potential
$\Box^2$	D'Alembertian operator
∇^2	Laplacian operator

List of Figures

1. Introduction

The understanding and accurate prediction of sound radiation associated with aircraft applications is of current interest. Recently, a great deal of attention has been directed to modeling the ultrahigh by-pass ratio turbo-fan engine (ducted propfan) due to its efficiency and shrouded propeller design. This engine has become attractive as an efficient component of future commercial transport aircraft. It is known that an unshrouded propeller generates an acoustic field which tends to radiate in the lateral direction. By housing the propeller in a shroud or duct (as in the ducted propfan), potential benefits of noise reduction exist since the duct provides a shield in the primary radiation direction. The ability to accurately model this propeller noise in both the ducted and unducted cases is of great importance. Modeling techniques such as computational fluid dynamics (CFD), finite element methods (FEM) and boundary integral techniques have been utilized to predict the acoustic benefits of the ducted propfan. Eversman [1] developed a finite element model for the generation, propagation and radiation of noise of a ducted fan. He also constructed a free-field propeller model compatible with the finite element formulation and conducted noise studies as presented in ref. [1]. Radiated field results for both the ducted and unducted propeller were obtained. Lan [2] and Buhler [3] developed separate prediction methods based on a boundary integral technique for the acoustic field generated by a propeller within a circular, rigid duct.

The presence of a duct or shroud was shown in all above studies to reduce the level of noise radiated from a propeller, at least in the primary radiation direction. With the presence of the shroud, an acoustically treated duct wall can also be utilized to further

increase the level of noise reduction obtained. The work of Kosanchick [4] was an extension of the work presented in refs. [2,3] and included an acoustically treated duct wall. Dunn, Tweed and Farassat [5] also presented a similar model of the acoustic field generated by a ducted propfan. Their boundary integral equation technique modeled acoustically treated walls, but only rigid wall results were presented in ref. [5]. The models in refs. [2-5] required fewer overall computations than the finite element technique since the boundary integral method only requires dealing with a surface integration along the duct as compared to finite element computations over the entire region of interest. However, the boundary integral technique cannot be applied if complex geometrical models or complex mean flows are involved.

As it is of great importance to develop accurate prediction methods of sound radiation from a ducted propeller, it is also of importance to understand the relationship between the duct geometry and source type in regard to noise reduction. The analysis in refs. [2-4] was modified and applied to a point source rather than a propeller model by Myers [6]. With a simpler source model, comparisons could be made between the boundary integral technique and the CFD approach. Özyörük and Long [7] utilized a finite-difference approach in solving this particular problem, and their results were found to be in agreement with those of ref. [6].

The studies previously discussed in refs. [1-6] dealt with only an axisymmetric duct configuration. However, rectangular duct configurations are often utilized for experimental inlet research. Thus, it is the purpose of the current work to develop a boundary integral technique similar to those in refs. [2-6] to describe radiation from a

monopole or point source placed within a rectangular duct. This particular duct geometry lacks symmetry and requires significantly greater computational effort than the problems previously discussed in refs. [2-4,6]. The source was restricted to be a monopole so that at least the incident field would be symmetric in form. The duct walls are assumed to be rigid and infinitesimally thin. The current work utilizes a scattering formulation which decouples the effects of the duct and source [2-6]. The scattered pressure is discontinuous across the walls of the duct. It is governed by a generalized wave equation with a source term that is proportional to its unknown jump across the duct walls. An integral representation for the solution of this in terms of this jump in scattered pressure across the duct surface is obtained. The scattered pressure jumps are then represented by two carefully chosen shape function expansions. The free-space pressure is used as the input data and the method of collocation is utilized to solve a system of algebraic equations for the coefficients of the shape function expansions. From these coefficients, the jump in scattered pressure along the duct surface is obtained and substituted into the original integral representation to obtain the scattered pressure. The total acoustic pressure is obtained through the sum of the free-space or incident pressure and the scattered pressure for a particular field point.

The remainder of this thesis discusses the formulation and validation of the boundary integral technique in its application to the rectangular duct with a monopole source at its center. In particular, Chapter 2 details the development of the governing boundary integral equation. Chapter 3 presents the numerical details necessary to accurately obtain the solution to the set of algebraic equations. The impact of the choice

of parameters on the solution is shown through a few example problems as discussed in Chapter 4.

2. Theory

This chapter presents the development of the governing equations required for the prediction of the acoustic field radiated from a source in a moving rectangular duct.

2.1 Integral Representation

An acoustic source in an infinitesimally thin, rigid, rectangular duct is examined. The rectangle is of length L, width 2b and height 2a as shown in Figure 1. A body-fixed cartesian coordinate system $\bar{X}$, placed at the center of the moving duct, and an inertially-fixed cartesian coordinate system $\bar{x}$, are used to describe the duct. The duct is assumed to be moving subsonically at velocity V, in the negative x_3 direction of the inertially-fixed frame. The objective is to obtain the acoustic field radiated to free space through the open ends of the duct.

By linearizing the ideal fluid equations of motion it can be shown that acoustic wave propagation in isentropic flow with no body forces is governed by the wave equation which can be written in the form

$$\Box^2 p_t \equiv \frac{1}{c^2}\frac{\partial^2 p_t}{\partial t^2} - \nabla^2 p_t = q(\bar{x},t) \qquad (2.1)$$

where p_t is the total acoustic pressure, $q(\bar{x},t)$ is the noise source, and c is the speed of sound in the fluid medium.

The total acoustic pressure is written in terms of incident and scattered acoustic pressure components as

$$p_t = p_i + p_s \qquad (2.2)$$

where p_i is the free-space pressure due to the monopole source alone and p_s is the augmentation of the incident pressure due to the presence of the rectangular duct. Through the use of this scattering formulation, the effects of the duct and noise source are decoupled and can be handled separately. The incident field satisfies

$$\Box^2 p_i = q(\bar{x},t) \tag{2.3}$$

It then follows that the scattered field must satisfy the homogeneous wave equation

$$\Box^2 p_s = 0 \tag{2.4}$$

The objective is to obtain an integral representation for the scattered field along with the appropriate boundary conditions at the duct surface and a radiation condition specifying that the scattered field is outgoing in the region exterior to the duct.

Let $f(\bar{x})=0$ describe the surface of the thin, rigid duct moving in a direction tangent to itself where f is defined such that $\nabla f = \hat{n}$ and $\hat{n}$ is the unit outward normal to the duct surface. The presence of the solid duct walls gives rise to a discontinuity in scattered pressure across the duct surface. Through the use of generalized derivatives and eqn.(2.4), it can be shown that the scattered pressure is a solution to the generalized wave equation

$$\overline{\Box}^2 p_s = \overline{\nabla} \cdot \left[\Delta p_s \hat{n} \delta(f)\right] \tag{2.5}$$

where $\delta(\bullet)$ is the Dirac delta function and Δp_s is the jump in scattered pressure across the duct surface [8]. The bars over the differential operators in eqn. (2.5) signify generalized differentiation. Equation (2.5) is a special form of the well-known Ffowcs Williams-Hawkings (FW-H) equation [8,9].

By solving eqn.(2.5) utilizing the free-space Green's function for the wave equation, an integral representation for p_s is obtained in the form

$$4\pi\, p_s(\bar{x},t) = -\frac{1}{c}\frac{\partial}{\partial t}\iint_{f=0}\left[\frac{\Delta p_s \cos\theta}{r|1-M_r|}\right]_{\tau^*} dS - \iint_{f=0}\left[\frac{\Delta p_s \cos\theta}{r^2|1-M_r|}\right]_{\tau^*} dS \qquad (2.6)$$

The details of the derivation of eqn. (2.6) are given in number of earlier publications [8] and therefore will not be repeated here. In eqn. (2.6), $r = |\bar{r}| = |\bar{x} - \bar{y}|$ is the magnitude of the radiation vector representing the distance from a source point at $\bar{y}$ on f=0 to an observer at $\bar{x}$; M_r is the component of the surface Mach number in the direction of the radiation vector; θ is the angle between $\bar{r}$ and the unit normal to the surface of the duct $\hat{n}$ at the source location; dS is the elemental area of the duct surface f=0. The integrands are evaluated at the emission time τ^* which is a solution to the retarded time equation

$$t - \tau - \frac{r}{c} = 0 \qquad (2.7)$$

There is only one solution τ^* for the retarded time equation since the duct is assumed to be moving subsonically through the fluid medium. Physically, τ^* is the emission time of signals generated by a source on the duct surface that are received by an observer at position $\bar{x}$ at time t.

By applying the appropriate boundary conditions to eqn. (2.6), an integral equation will be developed from which the unknown jump in scattered pressure Δp_s is determined over the surface of the duct. Once Δp_s is known, the scattered acoustic field for any position and time $(\bar{x},t)$ can be determined using eqn. (2.6) again.

The following details of the analysis are simplified if eqn. (2.6) is expressed in terms of the body-fixed coordinate system. To relate the observer and source positions in the body-fixed reference frame to the observer and source positions in the inertially-fixed reference frame, the following transformation is utilized:

$$\begin{aligned} \bar{X} &= \bar{x} + Vt\,\bar{i}_3 \\ \bar{Y} &= \bar{y} + V\tau\,\bar{i}_3 \end{aligned} \tag{2.8}$$

Here $\bar{i}_3$ is the unit vector in the 3-direction.

The analytical development of the boundary integral equation to follow can be carried out for an arbitrary incident pressure field p_i. However, computational complexities make it desirable to introduce some symmetry into the problem. Thus, at this stage it is assumed that the acoustic source is a monopole and, for further simplicity, it is positioned at the origin of the body-fixed coordinate system (i.e., at the center of the duct). Among other things, this restriction ensures that the scattered pressure jumps are identical on surfaces $x_2 = \pm b$ and $x_1 = \pm a$. The incident field corresponding to a moving monopole source is reviewed in the next section.

2.2 Incident Monopole Field

The incident field is the field due to the source alone without the presence of the duct. The solution to eqn. (2.3) can be obtained for the monopole source in terms of a complex velocity potential that satisfies

$$\Box^2\phi_i = \frac{1}{c^2}\frac{\partial^2\phi_i}{\partial t^2} - \nabla^2\phi_i = Ae^{-i\omega t}\delta(x_3 + Vt)\delta(x_2)\delta(x_1) \tag{2.9}$$

where A is defined as the source strength. The solution to eqn. (2.9) is well known and appears, for example, in Morse and Ingard [10]. In terms of the body-fixed coordinates the solution presented in [10] is

$$\phi(\bar{X},t) = \frac{-Ae^{-i\omega t}}{4\pi\sqrt{B_o}} \exp\left[i\alpha\left(\frac{-MX_3}{\beta} + \sqrt{B_o} \right) \right] \tag{2.10}$$

where the symbol α, which is used throughout this work, is defined by $\alpha = \omega/c\beta$, and $\beta^2 = 1 - M^2$. Use of the relation

$$p_i = -\rho_o \left.\frac{\partial\phi}{\partial t}\right|_{\bar{x}} = -\rho_o \left(\left.\frac{\partial\phi}{\partial t}\right|_{\bar{X}} + V\frac{\partial\phi}{\partial X_3} \right) \tag{2.11}$$

yields the incident monopole complex pressure field in the form

$$p_i = \frac{-\rho_o cA\, e^{-i\omega t}}{4\pi\beta^2} \left\{ \frac{i\alpha\left(\frac{-MX_3}{\beta} + \sqrt{B_o} \right)}{B_o} + \frac{\frac{MX_3}{\beta}}{(B_o)^{3/2}} \right\} e^{i\alpha\left(\frac{-MX_3}{\beta} + \sqrt{B_o} \right)} \tag{2.12}$$

where $B_o = \frac{X_3^2}{\beta^2} + X_1^2 + X_2^2$ and ρ_o is the fluid density. As noted above, the monopole complex pressure field expressed in eqn. (2.12) will be the only incident field considered here. As with all quantities in the following, the physical pressure is taken to be the real part of the complex incident pressure.

2.3 Boundary Integral Formulation

The analysis involved in formulating the boundary integral equation requires lengthy algebraic manipulations of eqn. (2.6) that are simplified if it is written in terms of the body-fixed coordinates. For convenience define ξ, η and ζ as

$$\xi = \frac{Y_3 - X_3}{\beta}, \qquad \eta = Y_2 - X_2, \qquad \zeta = Y_1 - X_1 \tag{2.13}$$

These abbreviations are utilized frequently throughout this work. The radiation vector, which extends from the duct surface f=0 to an observer at $\bar{x}$, is

$$\bar{r} = \bar{x} - \bar{y} = \bar{X} - \bar{Y} - V(t-\tau)\hat{i}_3 \tag{2.14}$$

Substitution of eqn. (2.14) into the retarded time equation eqn.(2.7), leads to a quadratic equation for the radiation distance at time τ^*, whose solution is

$$r^* = \frac{\left(M\xi + \sqrt{\xi^2 + \eta^2 + \zeta^2}\right)}{\beta} = c\left(t - \tau^*\right) \tag{2.15}$$

The component of the surface Mach number in the direction of the radiation vector is

$$M_r = M\vec{i}_3 \cdot \frac{\bar{r}}{r} = \frac{-\left[M\xi\beta + M^2 r\right]}{r} \tag{2.16}$$

where r is the magnitude of the radiation vector. Evaluation of eqn. (2.16) at the emission time τ^* and use of eqn. (2.15) yields

$$\left|1 - M_r\right|^* = \frac{\beta\sqrt{\xi^2 + \eta^2 + \zeta^2}}{r^*} \tag{2.17}$$

The factor $\cos\theta$ is given by

$$\cos\theta = \frac{\hat{n} \cdot \bar{r}}{r} \tag{2.18}$$

Finally, the scattered pressure jump Δp_s can be modeled in the form suggested by the incident field as

$$\Delta p_s\left(\bar{X}_s, t\right) = \pi\left(\bar{X}_s\right) e^{-i\omega t} e^{\frac{-i\alpha M X_3}{\beta}} \tag{2.19}$$

where $\bar{X}_s$ represents surface coordinates. Evaluation of eqn. (2.19) at the emission time gives

$$\Delta p_s\left(\bar{Y}_s,\tau^*\right)=\pi\left(\bar{Y}_s\right)e^{-i\omega t}e^{\frac{i\omega r^*}{c}}e^{\frac{-i\alpha MY_1}{\beta}} \qquad (2.20)$$

Substitution of eqns. (2.17), (2.18) and (2.20) into the two surface integrals representing the scattered pressure in eqn. (2.6), then puts the integral representation of p_s in the form

$$4\pi p_s(\bar{X},t)=-\frac{1}{c}\frac{\partial}{\partial t}\int_{f=0}\frac{\pi\left(\bar{Y}_s\right)\hat{n}\cdot\bar{r}\,e^{-i\omega t}e^{\frac{i\omega r^*}{c}}e^{\frac{-i\alpha MY_3}{\beta}}}{r^*\sqrt{\xi^2+\eta^2+\varsigma^2}}dS-\int_{f=0}\frac{\pi\left(\bar{Y}_s\right)\hat{n}\cdot\bar{r}\,e^{-i\omega t}e^{\frac{i\omega r^*}{c}}e^{\frac{-i\alpha MY_3}{\beta}}}{\left(r^*\right)^2\sqrt{\xi^2+\eta^2+\varsigma^2}}dS \qquad (2.21)$$

The time derivative of the first term in eqn. (2.21) is calculated at fixed $\bar{x}$. It can be obtained using the material derivative operator of eqn. (2.11). After algebraic manipulations, eqn. (2.21) can be rewritten as a single surface integral in the form

$$4\pi\beta p_s(\bar{X},t)=e^{-i\omega t}e^{\frac{-i\alpha MX_1}{\beta}}\int_{f=0}\pi\left(\bar{Y}_s\right)\hat{n}\cdot\bar{r}\left[\frac{i\alpha}{\xi^2+\eta^2+\varsigma^2}-\frac{1}{\left(\xi^2+\eta^2+\varsigma^2\right)^{3/2}}\right]\exp\left(i\alpha\sqrt{\xi^2+\eta^2+\varsigma^2}\right)dS \qquad (2.22)$$

Equation (2.22) is the integral representation of the scattered pressure written in terms of body-fixed coordinates. At this stage, eqn. (2.22) applies for an arbitrary duct cross-section.

In the next phase of the analysis, the incident field is utilized in conjunction with eqn. (2.22) to form the boundary integral equation. To accomplish this goal, a boundary condition is introduced for a duct with rigid walls. The no penetration condition is applied, namely $\bar{u}_t\cdot\bar{n}=0$ on the duct surface f=0. Substituting the no penetration boundary condition into the linearized momentum equation yields

$$\rho\frac{\partial\left(\bar{u}_t\cdot\bar{n}\right)}{\partial t}=-\frac{\partial p_t}{\partial n}=0 \qquad (2.23)$$

Then use of eqn. (2.2) implies that the boundary condition on the scattered pressure is

$$\frac{\partial p_s}{\partial n}=-\frac{\partial p_i}{\partial n} \qquad (2.24)$$

on the duct surface. Therefore, after taking the normal derivative of eqn. (2.22) and utilizing eqn. (2.24), it follows that

$$-4\pi\beta\frac{\partial p_i}{\partial n}(\bar{X},t)=e^{-i\omega t}e^{\frac{-i\alpha MX_1}{\beta}}\frac{\partial}{\partial n}\left\{\int_{f=0}\pi\left(\bar{Y}_s\right)\hat{n}\cdot\vec{r}\left[\frac{i\alpha}{\xi^2+\eta^2+\varsigma^2}-\frac{1}{\left(\xi^2+\eta^2+\varsigma^2\right)^{3/2}}\right]\exp\left(i\alpha\sqrt{\xi^2+\eta^2+\varsigma^2}\right)dS\right\} \tag{2.25}$$

in the limit as the observer at $\bar{X}$ approaches the duct surface f=0. Equation (2.25) is the boundary integral equation whose solution for the unknown jump amplitude π is the object of the remainder of this work.

The integral equation (2.25) is now specialized for the rectangular duct by noting that, due to the symmetry of the walls and the positioning of the acoustic source, the jumps in scattered pressure are identical for $X_1=\pm a$, i.e., the top and bottom surfaces, (see Figure 1) and similarly for $X_2=\pm b$, i.e., the two side surfaces. Thus, the jump amplitude π is defined separately for each independent surface as

$$\pi\left(\bar{X}_s,t\right)=\begin{Bmatrix}\pi_1(X_3,X_2) & \text{on} & X_1=\pm a\\ \pi_2(X_3,X_1) & \text{on} & X_2=\pm b\end{Bmatrix} \tag{2.26}$$

Further, the amplitudes π_1 and π_2 are represented as expansions in terms of shape functions to model the expected oscillatory behavior present on the surface of the duct. Thus π_1 and π_2 are written as

$$\begin{aligned}\pi_1(Y_3,Y_2)&=\sum_{j=0}^{J-1}\sum_{k=0}^{K1-1}a_{j,k}\varphi_j(Y_3)\psi_k(Y_2)\\ \pi_2(Y_3,Y_1)&=\sum_{j=0}^{J-1}\sum_{k=K1}^{K2+K1-1}a_{j,k}\varphi_j(Y_3)\psi_k(Y_1)\end{aligned} \tag{2.27}$$

where K_1, K_2 and J are the number of functions included to describe π on the surfaces $X_1=\pm a$ and $X_2=\pm b$ and along the length of the duct, respectively. The unknown coefficients $a_{j,k}$ in eqn. (2.27) are to be determined. The specific forms chosen for the

shape functions φ_j and ψ_k will be explored in detail in Chapter 3 of this thesis. The integral equation for the rigid, rectangular duct then appears in terms of contributions from each of its four sides in the form

$$-4\pi\beta\frac{\partial p_i(\bar{X},t)}{\partial n} = e^{-i\left(\omega t+\frac{\alpha M X_1}{\beta}\right)}\frac{\partial}{\partial n}\left\{\sum_{j=0}^{J-1}\sum_{k=0}^{K1-1}a_{j,k}\left[I_{j,k}^{(1)}+I_{j,k}^{(3)}\right]+\sum_{j=0}^{J-1}\sum_{k=K1}^{K1+K2-1}a_{j,k}\left[I_{j,k}^{(2)}+I_{j,k}^{(4)}\right]\right\} \qquad (2.28)$$

where

$$\begin{aligned}
I_{j,k}^{(1)} &= \int_{-L/2}^{L/2}\varphi_j(Y_3)\int_{-b}^{b}\psi_k(Y_2)(X_1-a)F(\xi,\eta,X_1-a)\,dY_2\,dY_3\\
I_{j,k}^{(2)} &= \int_{-L/2}^{L/2}\varphi_j(Y_3)\int_{-a}^{a}\psi_k(Y_1)(X_2-b)F(\xi,X_2-b,\zeta)\,dY_1\,dY_3\\
I_{j,k}^{(3)} &= -\int_{-L/2}^{L/2}\varphi_j(Y_3)\int_{-b}^{b}\psi_k(Y_2)(X_1+a)F(\xi,\eta,X_1+a)\,dY_2\,dY_3\\
I_{j,k}^{(4)} &= -\int_{-L/2}^{L/2}\varphi_j(Y_3)\int_{-a}^{a}\psi_k(Y_1)(X_2+b)F(\xi,X_2+b,\zeta)\,dY_1\,dY_3
\end{aligned} \qquad (2.29)$$

and where the function F is defined by

$$F(\xi,\eta,\zeta) = \left\{\frac{i\alpha}{\xi^2+\eta^2+\zeta^2}-\frac{1}{\left(\xi^2+\eta^2+\zeta^2\right)^{3/2}}\right\}\exp\left[i\alpha\left(\sqrt{\xi^2+\eta^2+\zeta^2}\right)\right] \qquad (2.30)$$

In solving eqn. (2.28) later it will be required that the integral equation be evaluated for observers on the top surface X_1=a and on the side surface X_2=b. The analysis here will be presented only for an observer positioned on the top surface, and it will be assumed that X_2 is on the interval $-b<X_2<b$ so that the observer is never precisely at the corner of the duct. The same type of analysis can also be utilized when an observer is positioned on the side surface of the rectangular duct. It is unnecessary to repeat the derivation however, because the result follows by analogy with that for the observer on the top surface by simply interchanging X_1 and X_2, Y_1 and Y_2, ζ and η, and a and b.

The normal (or X_1) derivatives indicated in eqn. (2.28) are now calculated to put the integral equation in its desired final form. The left-hand side of eqn. (2.28) follows from eqn. (2.12) evaluated on X_1=a as

$$\frac{\partial p_i(\bar{X},t)}{\partial X_1} = P_i^{(1)}(X_3)\, e^{\frac{-i\alpha M X_3}{\beta}} e^{-i\omega t} \qquad (2.31)$$

where

$$P_i^{(1)}(X_3) = \frac{\rho_o c A}{4\pi\beta^2} \frac{X_1}{(B_o)^{3/2}} e^{i\alpha\sqrt{B_o}} \left[\frac{3MX_3}{\beta}\left(1 - i\alpha\sqrt{B_o}\right) + i\alpha B_o \left\{ 1 - i\alpha\left(\frac{-MX_3}{\beta} + \sqrt{B_o} \right) \right\} \right]_{X_1=a} \qquad (2.32)$$

and B_o is as previously defined. The integrand in the term $I_{j,k}^{(1)}$ of eqn. (2.28) is singular when the observer and source points coincide (i.e., X_3=Y_3, X_2=Y_2, X_1=Y_1=a), but the other three terms in eqn. (2.28) are non-singular as long as $X_2 \neq b$. Since the integrals in eqn. (2.28) are to be evaluated numerically, the singularity in the first integral must be removed and treated analytically. Thus, the normal derivative of $I_{j,k}^{(1)}$ will only be written symbolically at this time. On the other hand, the normal derivative of the three non-singular terms can be calculated directly for X_1=a. The manipulations required are purely algebraic and, after dividing out the common exponential factor, the boundary integral equation becomes

$$-4\pi\beta\, P_i^{(1)} = K^{(1)} + K^{(2)} + K^{(3)} + K^{(4)} \qquad (2.33)$$

where

$$K^{(1)} = \lim_{X_1 \to a} \frac{\partial}{\partial X_1} \sum_{j=0}^{J-1} \sum_{k=0}^{K1-1} a_{j,k} I_{j,k}^{(1)} = \sum_{j=0}^{J-1} \sum_{k=0}^{K1-1} a_{j,k} \left\{ \lim_{X_1 \to a} \frac{\partial I_{j,k}^{(1)}}{\partial X_1} \right\} \qquad (2.34)$$

$$K^{(2)} = \lim_{X_1 \to a} \frac{\partial}{\partial X_1} \sum_{j=0}^{J-1} \sum_{k=K1}^{K1+K2-1} a_{j,k} I_{j,k}^{(2)} = -\sum_{j=0}^{J-1} \sum_{k=K1}^{K1+K2-1} a_{j,k} \int_{-L/2}^{L/2} \varphi_j(Y_3) \int_{-a}^{a} \psi_k(Y_1)(Y_1 - a)(X_2 - b) G(\xi, b - X_2, Y_1 - a)\, dY_1\, dY_3$$

$$K^{(3)} = \lim_{X_1 \to a} \frac{\partial}{\partial X_1} \sum_{j=0}^{J-1} \sum_{k=0}^{K1-1} a_{j,k} I_{j,k}^{(3)} = -\sum_{j=0}^{J-1} \sum_{k=0}^{K1-1} a_{j,k} \int_{L/2}^{L/2} \varphi_j(Y_3) \int_{-b}^{b} \psi_k(Y_2) \left[F(\xi, \eta, 2a) + 4a^2 G(\xi, \eta, 2a) \right] dY_2\, dY_3 \qquad (2.35)$$

$$K^{(4)} = \lim_{X_1 \to a} \frac{\partial}{\partial X_1} \sum_{j=0}^{J-1} \sum_{k=K1}^{K1+K2-1} a_{j,k} I_{j,k}^{(4)} = \sum_{j=0}^{J-1} \sum_{k=K1}^{K1+K2-1} a_{j,k} \int_{L/2}^{L/2} \varphi_j(Y_3) \int_{-a}^{a} \psi_k(Y_1)(Y_1 - a)(X_2 + b) G(\xi, b + X_2, Y_1 - a)\, dY_1\, dY_3$$

and where the function G is defined by

$$G(\xi, \eta, \zeta) = \left(\frac{3}{\left(\xi^2 + \eta^2 + \zeta^2\right)^{5/2}} - \frac{3i\alpha}{\left(\xi^2 + \eta^2 + \zeta^2\right)^{2}} + \frac{(i\alpha)^2}{\left(\xi^2 + \eta^2 + \zeta^2\right)^{3/2}} \right) e^{i\alpha\sqrt{\xi^2 + \eta^2 + \zeta^2}} \qquad (2.36)$$

In the following section, the singular term given in eqn. (2.34) will be treated analytically. The other three terms involve only non-singular integrals, and these will be evaluated numerically in the form in which they are presented in eqn. (2.35).

2.4 Singularity Analysis

The singular integral term that appears in eqn. (2.34) contains the integral defined in eqn. (2.29). If the symbol h is introduced, where $h=X_1-a$, it can be written as

$$\lim_{h \to 0} \frac{\partial I_{j,k}^{(1)}}{\partial h} = \lim_{h \to 0} \frac{\partial}{\partial h} \left\{ h \int_{-L/2}^{L/2} \varphi_j(Y_3) \int_{-b}^{b} \psi_k(Y_2) F(\xi, \eta, h)\, dY_2\, dY_3 \right\} \qquad (2.37)$$

Define $I_k(Y_3,h)$ to be the transverse, inner integral in eqn. (2.37) so that

$$I_k(Y_3, h) = \int_{-b}^{b} \psi_k(Y_2) F(\xi, \eta, h)\, dY_2 \qquad (2.38)$$

This single integral is considered first; it is singular when ξ, η and h vanish, which occurs when the observer point coincides with the source point on $X_1=a$. By expanding the integrand for small values of ξ, η and h, the following expression is obtained

$$\psi_k F = (A_0 + A_1 \eta) \left(\frac{-1}{(B)^{3/2}} + \frac{(i\alpha)^2}{2\sqrt{B}} \right) - \frac{A_2 \eta^2}{(B)^{3/2}} + O(1) \qquad (2.39)$$

in which $B = \xi^2 + \eta^2 + h^2$, and

$$A_o = \psi_k(X_2),\ A_1 = \psi'_k(X_2),\ A_2 = \frac{\psi''_k(X_2)}{2}$$

The singular terms shown explicitly in eqn. (2.39) are denoted as $(\psi_k F)_o$, and eqn. (2.38) is written as

$$I_k(Y_3,h) = \int_{-b}^{b}\left[\psi_k F - (\psi_k F)_o\right]dY_2 + \int_{-b}^{b}(\psi_k F)_o\, dY_2 \qquad (2.40)$$

The first integral in eqn. (2.40) is completely non-singular as ξ, η and h approach zero. The second involves only elementary integrations which can be evaluated analytically by changing the integration variable to $\eta=Y_2-X_2$. This results in

$$\int_{-b}^{b}(\psi_k F)_o\, dY_2 = \left[\frac{(i\alpha)^2}{2}A_o \log\left(\eta+\sqrt{\xi^2+\eta^2+h^2}\right) + \frac{A_1}{\sqrt{\xi^2+\eta^2+h^2}} + \frac{(i\alpha)^2}{2}A_1\sqrt{\xi^2+\eta^2+h^2} + \right.$$

$$\left. A_2\left(\frac{\eta}{\sqrt{\xi^2+\eta^2+h^2}} - \log\left(\eta+\sqrt{\xi^2+\eta^2+h^2}\right)\right) - \frac{A_o\eta}{(\xi^2+h^2)\sqrt{\xi^2+\eta^2+h^2}}\right]_{\eta_-}^{\eta_+} \qquad (2.41)$$

Here the η limits are defined by $\eta_-=-b-X_2$ and $\eta_+=b-X_2$; therefore, neither limit vanishes if $-b<X_2<b$ and only the last term on the right hand side of eqn. (2.41) is singular as ξ and h go to zero.

The expression in eqn. (2.40), including the result of eqn. (2.41), is now substituted back into eqn. (2.37). At this stage of the analysis, each of the non-singular integrals that appear can be differentiated with respect to h and the limit as h goes to zero can be calculated directly. This yields

$$\lim_{h\to 0}\frac{\partial I^{(1)}_{j,k}}{\partial h} = \int_{-L/2}^{L/2}\varphi_j(Y_3)\int_{-b}^{b}\left[\psi_k F - (\psi_k F)_o\right]_{h=0} dY_2\, dY_3$$

$$+ \int_{-L/2}^{L/2}\varphi_j(Y_3)\left[\frac{(i\alpha)^2}{2}A_o\log\left(\eta+\sqrt{\xi^2+\eta^2}\right) + \frac{A_1}{\sqrt{\xi^2+\eta^2}} + \frac{(i\alpha)^2}{2}A_1\sqrt{\xi^2+\eta^2} + A_2\left(\frac{\eta}{\sqrt{\xi^2+\eta^2}} - \log\left(\eta+\sqrt{\xi^2+\eta^2}\right)\right)\right]dY_3$$

$$-A_o \lim_{h\to 0} \frac{\partial}{\partial h}\left\{ h \int_{-L/2}^{L/2} \varphi_j(Y_3)\left[\frac{\eta}{(\xi^2+h^2)\sqrt{\xi^2+\eta^2+h^2}} \right]_{\eta_-}^{\eta_+} dY_3 \right\} \qquad (2.42)$$

The first two terms on the right in eqn. (2.42) can be evaluated numerically without difficulty, and will not be discussed further. The entire singular behavior of the boundary integral equation (2.33) has now been isolated in the third term, and this is the subject of the remainder of this section.

To further analyze the singular term in eqn. (2.42), define the function F_o as

$$F_0(\xi,h) = \left. \frac{\eta}{\sqrt{\xi^2+\eta^2+h^2}} \right|_{\eta_-}^{\eta_+} \qquad (2.43)$$

Since neither η_+ nor η_- vanish, the function F_o is non-singular when ξ=h=0. The third term on the right side of eqn. (2.42) is rewritten as

$$Q_s = -A_o \lim_{h\to 0} \frac{\partial}{\partial h}\{hI_s\} \qquad (2.44)$$

where

$$I_s = \int_{-L/2}^{L/2} \frac{\varphi_j(Y_3)\, F_0(\xi,h)}{\xi^2+h^2} dY_3 \qquad (2.45)$$

Given F_o as defined in eqn. (2.43), define a sequence of functions F_m according to

$$F_m(\xi,h) = F_m(0,h) + \xi\, F_{m+1}(\xi,h) \qquad (2.46)$$

for m=0,1,2,... . After use of eqn. (2.46) with m=0, I_s can be expressed as

$$I_s = F_0(0,h) \int_{-L/2}^{L/2} \frac{\varphi_j(Y_3)}{\xi^2+h^2} dY_3 + \int_{-L/2}^{L/2} \frac{\xi F_1(\xi,h)\varphi_j(Y_3)}{\xi^2+h^2} dY_3 \qquad (2.47)$$

Because the second term of eqn. (2.47) is still singular when h=0, eqn. (2.46) is applied again with m=1 which yields

$$I_s = F_0(0,h)\int_{-L/2}^{L/2}\frac{\varphi_j(Y_3)}{\xi^2+h^2}dY_3 + F_1(0,h)\int_{-L/2}^{L/2}\frac{\xi\varphi_j(Y_3)}{\xi^2+h^2}dY_3 + \int_{-L/2}^{L/2}\frac{\xi^2 F_2(\xi,h)\varphi_j(Y_3)}{\xi^2+h^2}dY_3 \qquad (2.48)$$

The third integral in eqn. (2.48) is now non-singular at h=0.

From eqn. (2.46) it follows that

$$F_1(0,h) = \lim_{\xi\to 0}\left[\frac{F_o(\xi,h)-F_o(0,h)}{\xi}\right] = \frac{\partial F_o(0,h)}{\partial\xi} = 0 \qquad (2.49)$$

In addition, making use of the fact that $\beta\xi=Y_3-X_3$, it is seen that the first integral in eqn. (2.48) can be rewritten as

$$\int_{-L/2}^{L/2}\frac{\varphi_j(Y_3)dY_3}{\xi^2+h^2} = -\frac{\beta}{h}\frac{\partial}{\partial X_3}\int_{-L/2}^{L/2}\varphi_j(Y_3)\tan^{-1}\left(\frac{\xi}{h}\right)dY_3 \qquad (2.50)$$

It then follows that

$$\lim_{h\to 0}\frac{\partial}{\partial h}(hI_s) = \lim_{h\to 0}\frac{\partial}{\partial h}\left\{-\beta F_0(0,h)\frac{\partial}{\partial X_3}\int_{-L/2}^{L/2}\varphi_j(Y_3)\tan^{-1}\left(\frac{\xi}{h}\right)dY_3 + h\int_{-L/2}^{L/2}\frac{\xi^2 F_2(\xi,h)\varphi_j(Y_3)}{\xi^2+h^2}dY_3\right\} \qquad (2.51)$$

The limits in eqn. (2.51) can now be evaluated. The first term on the right is

$$\lim_{h\to 0}\left\{-\beta\frac{\partial F_o(0,h)}{\partial h}\frac{\partial}{\partial X_3}\int_{-L/2}^{L/2}\varphi_j(Y_3)\tan^{-1}\left(\frac{\xi}{h}\right)dY_3 + \beta F_o(0,h)\frac{\partial}{\partial X_3}\int_{-L/2}^{L/2}\frac{\xi\varphi_j(Y_3)}{\xi^2+h^2}dY_3\right\}$$

$$= \lim_{h\to 0}\left\{\beta\frac{\partial F_o(0,h)}{\partial h}h\int_{-L/2}^{L/2}\frac{\varphi_j(Y_3)}{\xi^2+h^2}dY_3 + \beta F_o(0,h)\frac{\partial}{\partial X_3}\int_{-L/2}^{L/2}\frac{\xi\varphi_j(Y_3)}{\xi^2+h^2}dY_3\right\} \qquad (2.52)$$

after differentiation. The first term on the right hand side of eqn. (2.52) can yield a non-zero limit only because of contributions of the integral at the singular point $\xi=0$. The limit is therefore obtained by reducing the integration range to small local interval $-\delta<\xi<\delta$ so that it becomes

$$\lim_{h\to 0}\left\{h\frac{\partial F_o(0,h)}{\partial h}\varphi_j(Y_3)\int_{-\delta}^{\delta}\frac{1}{\xi^2+h^2}dY_3\right\} = \lim_{h\to 0}\left\{\frac{\partial F_o(0,h)}{\partial h}\varphi_j(X_3)\tan^{-1}\left(\frac{\xi}{h}\right)_{-\delta}^{\delta}\right\} = 0 \qquad (2.53)$$

because $\partial F_o/\partial h$ vanishes at h=0. The second term on the right of eqn. (2.52) is expressible in terms of a Cauchy principal value integral as

$$I_j^{(pv)} = 2\beta \frac{\partial}{\partial X_3} \int\!\!\!\!\!\!-_{-L/2}^{L/2} \frac{\varphi_j(Y_3)}{\xi} dY_3 \tag{2.54}$$

after using the fact that $F_o(0,0)=2$.

Now, consider the second term on the right side of eqn. (2.51). It is

$$\lim_{h\to 0} \frac{\partial}{\partial h} \left\{ h \int_{-L/2}^{L/2} \frac{\xi^2 F_2(\xi,h)\varphi_j(Y_3)}{\xi^2+h^2} dY_3 \right\} = \int_{-L/2}^{L/2} F_2(\xi,0)\varphi_j(Y_3)\,dY_3 + \lim_{h\to 0}\left\{ h \int_{-L/2}^{L/2} \frac{\xi^2}{\xi^2+h^2}\left[\frac{\partial F_2(\xi,h)}{\partial h} - \frac{2hF_2(\xi,h)}{\xi^2+h^2} \right]\varphi_j(Y_3)\,dY_3 \right\} \tag{2.55}$$

It is easily shown, by the same procedure that led to eqn. (2.53), that the local contribution of the second term in eqn. (2.55) also vanishes.

Finally, because

$$F_2(\xi,0) = \frac{F_o(\xi,0) - F_o(0,0) - \xi F_1(0,0)}{\xi^2} = \frac{F_o(\xi,0) - F_o(0,0)}{\xi^2} \tag{2.56}$$

it follows from eqn. (2.55) and (2.56) that eqn. (2.44) is

$$Q_s = -A_o \lim_{h\to 0} \frac{\partial}{\partial h}(hI_s) = -A_o \left\{ 2\beta \frac{\partial}{\partial X_3} \int\!\!\!\!\!\!-_{-L/2}^{L/2} \frac{\varphi_j(Y_3)}{\xi} dY_3 + \int_{-L/2}^{L/2} \frac{\varphi_j(Y_3)}{\xi^2} \left\{ \frac{\eta}{\sqrt{\eta^2+\xi^2}}\Big|_{\eta_-}^{\eta_+} - \frac{\eta}{|\eta|}\Big|_{\eta_-}^{\eta_+} \right\} dY_3 \right\} \tag{2.57}$$

where η_+ and η_- are as previously defined. The shape functions φ_j will be defined in the following chapter of this thesis and it will be shown there that an analytical expression for the Cauchy principal value integral can be obtained. It should be emphasized here that the second integral in eqn. (2.57) is non-singular and can be evaluated numerically without any difficulty.

2.5 Summary

At this point it is appropriate to summarize the lengthy analysis just presented. Equation (2.33) is the singular integral equation to be solved for the unknowns $a_{j,k}$. To solve this equation numerically requires the evaluation of the integrands that appear as coefficients of the unknowns in eqns. (2.34) and (2.35). However, the singular integral of eqn. (2.34) cannot be evaluated directly. The preceding section has outlined the method by which the singularity has been removed from the integral. Its complete analytical evaluation will be carried out in the following chapter. The numerical task remaining involves only the straightforward evaluation of the double integrals in eqn. (2.35), the double integral in the first term on the right in eqn. (2.42), the single integral in the second term on the right in eqn. (2.42) and the single integral in the second term on the right in eqn. (2.57). Again, all of these integrals are non-singular and can be evaluated numerically without difficulty. As mentioned previously, all of these expressions can be converted to apply to an observer on the side surface by the appropriate interchange of variables.

The next chapter outlines the numerical procedure followed to obtain the unknowns $a_{j,k}$ which determine the unknown scattered pressure jump across the duct walls. Once known they are utilized to calculate the scattered pressure at an arbitrary $\bar{X}$ in the field from

$$p_s(\bar{X},t) = \frac{e^{-i\left(\omega t+\frac{\alpha M X_1}{\beta}\right)}}{4\pi\beta}\left\{\sum_{j=0}^{J-1}\sum_{k=0}^{K1-1} a_{j,k}\left[I_{j,k}^{(1)} + I_{j,k}^{(3)}\right] + \sum_{j=0}^{J-1}\sum_{k=K1}^{K1+K2-1} a_{j,k}\left[I_{j,k}^{(2)} + I_{j,k}^{(4)}\right]\right\} \qquad (2.58)$$

where the $I_{j,k}^{(\cdot)}$ are the integrals defined in eqn. (2.29); all of these integrals are non-singular so long as $\bar{X}$ is not on the duct surface. The total acoustic pressure radiated from the duct is obtained by addition of the known incident pressure to the calculated scattered pressure.

3. Numerical Implementation

The previous chapters detailed the development of the set of equations which, when solved, predict the acoustic field generated by a monopole source placed at the center of a rectangular duct. The equations have been analytically treated to eliminate problems in implementing numerical schemes. The governing equations for this problem have been coded into a FORTRAN code and run on a 500MHz DEC-Alpha workstation.

Before addressing the issues in this chapter it is pointed out that the axial integration in eqn. (2.33) is similar to that done by Kosanchick [4] in applying a boundary integral technique to predict the acoustic field generated by propellers in lined as well as rigid circular ducts. A shape function expansion was also posed there for the axial behavior of the scattered pressure jump along the surface of the duct. However, the form of the expansion proved to require adaptive techniques at the leading and trailing edges of the duct due to sensitivity to the choice of parameters. The code developed for the rigid circular cylinder was later modified to replace the propeller noise source model with a point monopole. Results describing radiation from the monopole acoustic source were discussed by Myers [6]. Prior to the current consideration of the rectangular duct, a new set of shape functions were introduced to describe scattered pressure jump along the surface of the circular duct. Through extensive numerical testing, it was found that this new set of shape functions eliminated the need for additional adaptive techniques at the leading and trailing edges of the duct. The current analysis for the rectangular duct makes use of this new set of axial shape functions and they are discussed in the following section of this chapter.

3.1 Pressure Jump Representation

The scattered pressure jumps are represented as a series of products of two sequences of carefully chosen shape functions as presented in eqn.(2.27). The shape function expansions are chosen to model the oscillatory behavior expected on the duct surface as well as the appropriate behavior of the pressure jump at the leading and trailing edges of the duct. With these criteria in mind, the shape function expansion for the axial direction is discussed first.

It is known that integral equations like the one under consideration here do not have unique solutions until further conditions associated with the edge behavior of the solution are specified. As in thin airfoil theory, the pressure jump that satisfies eqn. (2.33) can be expected to have an inverse square-root singularity at the leading edge of the duct when $M \neq 0$, and a square-root zero is anticipated at the trailing edge of the duct [11]. This latter condition is the well known Kutta condition. These edge conditions can best be imposed by introducing the variable

$$Y_3 = -\frac{L}{2}\cos\kappa \tag{3.1}$$

where $0 \leq \kappa \leq \pi$, and by defining

$$X_3 = -\frac{L}{2}\cos\kappa_o \tag{3.2}$$

Now, the axial variation of the scattered pressure jump is written in terms of the set of functions commonly utilized in thin airfoil theory [11]:

$$\varphi_j(\kappa) = \begin{cases} \dfrac{1+\cos\kappa}{\sin\kappa} & j = 0 \\ \sin j\kappa, & j = 1,\ldots,J-1 \end{cases} \tag{3.3}$$

The leading edge singularity at $\kappa=0$ is contained explicitly in the first term of the sequence. It is easily shown using eqn. (3.1) that it grows as the inverse square root of distance from the edge. The remaining terms vanish at the leading edge of the duct and all vanish as the square root of distance from the trailing edge in accordance with the Kutta condition. As mentioned previously, use of eqn. (3.3) with a uniform discretization in κ rather than Y_3, has been shown to eliminate the need for additional adaptive techniques in handling the square root singularity at the leading edge of the duct. Most importantly, the Cauchy principal value integral of eqn. (2.54) can be obtained analytically for the shape function expansion posed in eqn. (3.3). This analytical result will be discussed in the next section.

The variation in the scattered pressure jump in the lateral direction on the wall surfaces is expected to be similar to that seen in the incident pressure field. This variation can be replicated by a sequence of functions that are sinusoidal in form. Therefore, the shape functions modeling the lateral oscillations of the jump on the surfaces of the duct are taken in the form

$$\psi_k(Y_2) = \begin{cases} 1 & k = 0 \\ \sin\left[(2k-1)\pi\left(\dfrac{Y_2+b}{2b}\right)\right] & k = 1, \ldots, K_1 - 1 \end{cases} \tag{3.4}$$

and

$$\psi_k(Y_1) = \begin{cases} 1 & k = K_1 \\ \sin\left[(2k-2K_1-1)\pi\left(\dfrac{Y_1+a}{2a}\right)\right] & k = K_1+1, \ldots, K_1+K_2-1 \end{cases} \tag{3.5}$$

where K_1 and K_2 are the finite number of functions to be used in the sequences. Both sets of functions are symmetric about the midpoints of their respective lateral surfaces.

It is noted that only a finite number of functions are used. Choosing the correct number of functions from each shape function expansion set is not a straightforward task. The number of functions that is sufficient for an accurate solution varies depending on the choice of problem parameters such as Mach number, frequency and length of duct in relation to the cross-sectional geometry. The process of determining the proper number of functions is discussed later in conjunction with a numerical discussion of a sample problem.

3.2 Principal Value Integral

The Cauchy principal value that appears in eqn. (2.57) can be evaluated analytically for the shape functions defined in eqn. (2.33). By utilizing the relation $\beta\xi=Y_3-X_3$, and the transformation of eqn. (3.1), the integral becomes

$$I_j^{(pv)} = 2\beta^2 \frac{\partial}{\partial X_3} \int_{-L/2}^{L/2} \frac{\varphi_j(Y_3)}{(Y_3 - X_3)} dY_3 = -2\beta^2 \frac{\partial}{\partial X_3} \int_0^{\pi} \frac{\varphi_j(\kappa)}{\cos\kappa - \cos\kappa_o} \sin\kappa d\kappa \qquad (3.6)$$

The shape functions are substituted into eqn. (3.6) and the known integral

$$\int_0^{\pi} \frac{\cos n\kappa}{\cos\kappa - \cos\kappa_o} d\kappa = \frac{\pi \sin n\kappa_o}{\sin\kappa_o} \qquad (3.7)$$

derived, for example, by Karamcheti [11], is used. For j=0 this yields

$$I_o^{(pv)} = -2\beta^2 \frac{\partial}{\partial X_3} \int_0^{\pi} \frac{1+\cos\kappa}{(\cos\kappa - \cos\kappa_o)} d\kappa = -2\beta^2 \frac{\partial}{\partial X_3}[0+\pi] = 0 \qquad (3.8)$$

When j>0, eqn. (3.6) is

$$I_j^{(pv)} = -2\beta^2 \frac{\partial}{\partial X_3} \int_0^{\pi} \frac{\sin j\kappa \sin\kappa}{(\cos\kappa - \cos\kappa_o)} d\kappa \qquad (3.9)$$

Utilizing the trigonometric identity

$$\sin j\kappa \sin \kappa = \frac{\cos(j-1)\kappa - \cos(j+1)\kappa}{2} \tag{3.10}$$

and the relation established in eqn. (3.7), eqn. (3.9) is

$$I_j^{(pv)} = 2\beta^2 \frac{\partial}{\partial X_3}\left(\pi \cos j\kappa_o\right) = \frac{-4\pi\beta^2 j}{L} \frac{\sin j\kappa_o}{\sin \kappa_o} \tag{3.11}$$

where eqn. (3.2) has been utilized to obtain the derivative with respect to X_3. The results expressed in eqns. (3.8) and (3.11) constitute, in analytical form, the entire effect of the singularities in the integral equation (2.33).

3.3 Method of Collocation

Given a choice of the number of shape functions J, K_1, and K_2, there are a total of $J(K_1+K_2)$ unknown coefficients $a_{j,k}$ to be determined to complete the solution of eqn. (2.33). Although there are numerous techniques available, the method of collocation [12] is the technique utilized here to obtain the solution. This method involves the selection of a grid of observer points on the surface at which the integral equation eqn. (2.33) is satisfied exactly, thus producing a set of inhomogeneous linear algebraic equations for the unknown coefficients. In the current work, however, the method is supplemented by imposing the obvious physical condition that the pressure jumps on each wall should equal one another at the corners where the walls meet. Thus, for example, it will be required that $\pi_1(X_3,b) = \pi_2(X_3,a)$. If an unlimited number of functions were used in each series expansion, this condition would presumably not be necessary. However, the constraint imposed by the corner condition has been found to lead to an accurate representation of the jump in scattered pressure using what appears to be as few shape functions as possible.

The grid of observer points used here consists of J locations evenly distributed along the X_3 direction of the surface over the interval $-L/2 < X_3 < L/2$. Because of the symmetry present in the current problem, only one quarter of the perimeter of the duct must be considered. Thus, K_1 evenly distributed observer locations are chosen over the interval $0 \leq X_2 < b$ on the top surface, and K_2-1 locations are distributed over $0 \leq X_1 < a$ on the side. The integral equation is satisfied at these $J(K_1+K_2-1)$ points. The remaining J equations necessary to complete the algebraic system are obtained by imposing the corner condition at the J axial stations of the grid.

The first and last axial collocation locations are at a distance D^* in from the leading and trailing edges of the duct. The first grid point for each side is placed at the center of each side (i.e., $X_2=0$, $X_1=0$) and the last is chosen at a distance of 10% of the half length of the side in from the corner.

3.4 Numerical Integration

With the set of collocation points defined, the numerical evaluations of the integrals of eqn. (2.34) is discussed. Four point Gauss-Legendre Quadrature is utilized to complete all of the necessary integrations [12,13]. The integrands in eqn. (2.34) are all non-singular and are well behaved and can be numerically integrated accurately given that the proper discretization is utilized. The discretizations required along Y_2 and Y_1 are independently determined based on the oscillatory behavior of the integrands. For the surfaces $X_1 = \pm a$, the oscillations of the integrand are governed by the shape functions $\psi_k(Y_2)$ and the exponential function in terms of ξ and η as

$$\sin\left[(2k-1)\pi\left(\frac{Y_2+b}{2b}\right)\right]e^{i\alpha\sqrt{\xi^2+\eta^2+\zeta^2}} \qquad (3.12)$$

The Y_2 oscillations are most rapid when ξ=0 and ζ=0. If the sine term in eqn. (3.12) is rewritten in exponential form, the fastest oscillatory behavior with respect to Y_2 is

$$e^{\left(i(2k-1)\pi\left(\frac{Y_2+b}{2b}\right)+i\alpha(Y_2-X_2)\right)} = e^{i\left(\frac{(2k-1)\pi}{2b}+\alpha\right)Y_2}e^{i\left(\frac{(2k-1)\pi}{2}-\alpha X_2\right)} \qquad (3.13)$$

Therefore, the wavelength of the fastest oscillation is

$$\lambda_s = \frac{2\pi}{\alpha+\frac{(2k-1)}{2b}\pi} \qquad (3.14)$$

The total number of panels along the $X_1 = \pm a$ surface is calculated using

$$N_s = P_\lambda \frac{2b}{\lambda_s} \qquad (3.15)$$

where P_λ is the number panels chosen per wavelength. This parameter allows for the optimization of the level of discretization utilized. Two panels per wavelength were chosen. The same procedure determines the most rapid variation in the oscillatory behavior of the integrand in eqn. (2.34) on the surfaces $X_2 = \pm b$.

The axial discretization for the Y_3 integration of all of the functions expressed in eqn. (2.33) is examined now. The relationship between the variables Y_3 and κ was established in eqn. (3.1). Utilizing an even distribution of integration points in κ leads to a clustering of integration points in Y_3 around the leading and trailing edges of the duct eliminating the need for additional adaptive techniques. The length of the duct is discretized evenly in κ on the interval $[0,\pi]$. The variation in the axial direction is described by

$$\sin j\kappa\, e^{i\alpha\sqrt{\xi^2+\eta^2+\zeta^2}} \tag{3.16}$$

The oscillations in κ are most rapid when η=0 and ζ=0. If the sine term in eqn. (3.16) is written in exponential form and ξ is written in terms of κ, then the most rapid variation in the axial direction is approximated by

$$e^{i\alpha\xi}e^{ij\kappa} \approx e^{i\left(\frac{L}{2}\alpha+j\right)\kappa} \tag{3.17}$$

Now the wavelength of the fastest oscillation is determined by

$$\lambda_\kappa = \frac{2\pi}{\alpha\frac{L}{2}+j} \tag{3.18}$$

The total number of panels required for the integration in the axial direction is calculated using

$$N_\kappa = P_\lambda \frac{\pi}{\lambda_\kappa} \tag{3.19}$$

where again, P_λ is the number of panels per wavelength. Four panels per wavelength are used for all of the axial integrations. The integration with respect to Y_3 is rediscretized for every j and, likewise, the integration with respect to either Y_1 or Y_2 is rediscretized for every k. The goal is to utilize as coarse a discretization as possible while maintaining a uniform level of accuracy. The testing of the accuracy of the level of integration utilized will be explored in the following section.

At this point, the numerical techniques necessary to obtain the solution to the integral equation in eqn. (2.33) have been described. In the next section the solution of a sample problem is investigated.

3.5 Sample Problem Solution

The previous sections outlined the methodology necessary to determine the acoustic field generated by a monopole source placed in a rectangular duct. The methodology is applied here to a sample problem to test the integrity of the FORTRAN code. The following table indicates the parameters chosen for the sample problem:

Parameter	Value	Parameter	Value
M	0.0	a	0.25 m
L	0.5 m	b	0.5 m
Frequency	750 Hz	c	340.17 m/sec

Here, the frequency and duct dimensions are relatively small in order to minimize the numerical effort required for the testing, and the duct and source are stationary in the fixed medium. In this case, the incident field is symmetric in the axial direction about X_3=0 and therefore the jump in scattered pressure is also expected to be symmetric about X_3=0. Also, when M=0.0 there is no singularity in scattered pressure at the leading edge of the duct. Thus, for this test case, the coefficients of the singular first terms and the terms that are anti-symmetric about X_3=0 (j=2,4,6...) in the axial shape function expansions (2.27) must be driven to zero in the solution of the algebraic system that results from collocation.

The incident monopole pressure field is illustrated in Figures 2-4. Figure 2 shows the axial variation in the complex incident pressure amplitude in both real and imaginary parts on the duct surface X_1=a along its centerline X_2=0. The complex incident pressure amplitude for the lateral centerline X_3=0 is shown in Figure 3 for the surface X_1=a and is shown in Figure 4 for the surface X_2=b .

The method of collocation is now used to solve for the coefficients $a_{j,k}$ in eqn. (2.33). The grid of collocation locations is as discussed in section 3.3, and the axial offset D* is taken to be 0.1L. Assuming that the collocation grid is adequate and that the discretization discussed in section 3.4 yields accurate integrals, the number of functions from the expansions (2.27) required to ensure a converged solution must be determined. The oscillatory nature of the incident data function $P_i^{(1)}(X_3)$ in eqn. (2.33) dictates the number of functions required. However, this data function oscillates in a manner similar to that of the incident pressure so that the number of functions required can be inferred from the oscillations in the real and imaginary parts of the incident pressure illustrated in Figures 2-4. It is seen in Figure 2 that about 1 ½ oscillations exist in the incident pressure along the length of the duct for the sample problem. Experience indicates that it is necessary to include all terms in the expansions (2.27) up to terms that oscillate at least twice as fast as the incident data [4]. The axial shape functions (3.3) for $j \geq 1$ each have j half-oscillations over the length of the duct. Therefore, a minimum of 6 of these sine functions are expected to be required to reproduce the 1 ½ wavelengths (J=7). A total of 8 functions are actually chosen. Similar considerations determine K_1 and K_2 from the incident pressure amplitude plotted along the lateral centerlines $X_3=0$ on the surfaces $X_1=a$ and $X_2=b$. These lead to the choices $K_1=8$ and $K_2=6$. Upon solving eqn. (2.33), the coefficients $a_{j,k}$ are obtained from which the scattered pressure jump is calculated utilizing eqn. (2.27). The resulting pressure jump amplitude π_1 along $X_2=0$ on the surface $X_1=a$ is shown in Figure 5. It is seen that, as expected, the jump amplitude is symmetric about $X_3=0$ and there is no singularity present at the leading edge of the duct. Thus the scheme

has driven the singular terms and the anti-symmetric terms in the expansions (2.27) to zero as required. The jump amplitude π_1 on the surface X_1=a laterally along X_3=0 is shown in Figure 6 and the jump amplitude π_2 on the surface X_2=b along X_3=0 is shown in Figure 7. In Figures 5,6 and 7 the jump amplitudes are all smooth and, as expected, display oscillatory behavior similar to that of the corresponding plot of the incident field.

To determine if the solution obtained is converged, the number of functions used in the expansions (2.27) is varied. First, K_1 and K_2 are held constant and J is varied as shown in Figure 8. As J is increased there is little change in the scattered pressure jump. A conclusion can be made here that a sufficient number of axial shape functions were chosen. The same procedure is followed for the lateral functional expansions. Figures 9 and 10 show only minor changes when holding J=8 and varying the values of K_1 and K_2 for the X_3=0 lateral plane on the surface X_1=a and on the surface X_2=b, respectively. Therefore, it can be concluded that using J=8, K_1=8 and K_2=6 is sufficient to accurately represent the solution for the jump amplitude in this case. Further tests involving increasing all three parameters simultaneously were carried out, and all supported the same conclusion.

It is also necessary to verify the validity of the discretization utilized. This can be achieved by either increasing the number of Gauss points or by increasing the number of panels per wavelength, P_λ. Here the number of Gauss points is doubled from 4 points to 8 points. Figures 11 and 12 show that no apparent differences exist between results with the 4 point and 8 point Gauss-Legendre schemes along the lines X_2=0 and X_3=0 on the surface X_1=a. Many other such plots were examined, and all indicated that the level of

discretization utilized was sufficient to obtain accurate results. The remainder of the results presented in this thesis are obtained utilizing the 4 point Gauss-Legendre scheme with P_λ=2 for discretizing X_1 and X_2 and P_λ=4 when discretizing in X_3.

Finally, the choice of collocation points is considered. The collocation points are evenly distributed along the length of the duct and along half of each lateral side. The axial locations are distributed evenly between points at a fixed distance D* in from each end of the duct. A different set of collocation points results simply by changing the value of D*. Figure 13 shows that the solution with D*=0.005L exhibits no significant variations from the solution with D*=0.01L along the axial centerline of the surface X_1=a. Other points with varying D* values showed little variation in the solution as well. Similarly, the first lateral collocation points are on the center of each side and the last is placed at a distance 10% of the half-length of the respective side. The set of collocation points is modified by changing the position of the last point. The last collocation point was placed at a distance of either 9% or 11% of the half-length of the lateral surfaces. Figure 14 shows only slight changes in the solution when the set of collocation points is altered. The distance corresponding to 10% of the half-length is deemed reasonable since variations as small as these seen in Figure 14 have an insignificant effect on the radiated field which is the topic of the next chapter.

It should also be mentioned here that if the dimensions a and b were taken to be equal then, upon solving the system of equations, the jump amplitudes π_1 and π_2 should be identical. When the parameters selected for the sample problem were utilized in conjunction with the condition that the dimension a was the same as dimension b, the

jump amplitudes were found to be the same as expected. The same result was obtained when the observer points were taken on one surface and thereby reducing the number of unknowns.

3.6 Moving Duct Problem

While the problem discussed in the previous section was a useful test case, it is also of interest to examine the solution for the jump amplitude when the duct is in motion so that the jump is singular at the duct leading edge. Therefore, a case for which M=0.1 is presented here. The same numerical tests were also carried out for this case and led to similar conclusions in regard to the accuracy of the level of discretization as well as the choice of collocation locations. They will not be discussed further. For the moving case, the same parameters as utilized in the previous problem were retained except that the duct length was taken to be 2m. This is four times the length used in the sample problem and therefore 4 times as many sine functions in the axial shape function expansion would be expected to be required to obtain an accurate solution. However, for this flow case 25 functions from the expansion (2.27) were not sufficient. In fact, it was found that a total of 52 axial functions were required before the solution was completely converged. It appears that the need for so many functions arises because, in contrast to the circular duct treated in ref. [6], the singularity at the leading edge varies in strength around the perimeter of the duct. This differs significantly from the circular case where the singularity was determined by a single point at the leading edge of the duct. This is one reason why the rectangular duct problem is much more computationally intensive than

the circular case treated in ref. [6]. A total of K_1=8 and K_2=6 functions from the lateral surface expansions were found to be sufficient and no apparent change in the solution was observed when these values were varied. Figure 15 shows the scattered pressure jump on the surface X_1=a along X_2=0 for a rectangular duct in the presence of flow. Notice the square-root singularity at the leading edge of the duct and the square-root zero at the trailing edge of the duct.

The radiated field for the above sample problems, as was well as for a higher frequency case are presented in the next chapter.

4. Radiated Field

The previous chapters outlined the analysis necessary to determine the acoustic field generated by a monopole source placed at the center of a rectangular duct and some of the numerical checks made on the analysis for inconsistencies. Once the jump amplitudes π_1 and π_2 have been determined, the scattered pressure at any observer location is obtained by substituting these jump amplitudes into eqn. (2.22). The total pressure at any point in the field is then obtained through the simple addition of the incident and scattered pressure at an observer point in the field. The actual or physical pressure for the incident, scattered or total pressure is the real part of its complex counterpart. The corresponding root-mean squared (RMS) pressure is calculated in the usual manner such that

$$p_{rms} = \sqrt{\frac{pp^*}{2}} \tag{4.1}$$

where p^* is the complex conjugate of p. The sound pressure level (SPL) is determined by

$$SPL = 20\log\left(\frac{p_{rms}}{p_{ref}}\right) \tag{4.2}$$

where $p_{ref}=2 \times 10^{-5}$ Pa.

The incident, scattered and total pressures are illustrated in the following results one cross-sectional plane at a time on the intersection of a sphere centered at the origin of the body-fixed coordinate system and the plane of interest. These intersections are circles along which are given polar plots or directivities of the radiated field about the plane of

interest in terms of sound pressure levels in decibels (dB) from eqn. (4.2). A radius R of 5m was utilized for all of the directivities presented in this thesis. Figures 16(a)-(c) depict the center planes of interest. The directivity angle is called θ in each case, and it is measured from the positive X_n axis ($0°<\theta<180°$). This angle is utilized to obtain directivity plots for planes that intersect the source so that the radius of the arc for these polar plots is 5m. For planes that do not intersect the source, such as that shown in Figure 16(d), the radius of the polar arc is less than 5m. Since the incident field is spherically symmetric when M=0, repeated use of the same spherical radius leads to an incident field that is the same for each directivity plot for this case.

Chapter 3 included a detailed numerical validation process as well as the presentation of the jump amplitudes for the sample problem. The radiated field plots for the sample problem in the center planes $X_2=0$, $X_3=0$, and $X_1=0$ are presented as solid lines in Figures 17 (plane in Figure 16(a)), 18 (plane in Figure 16(b)) and 19 (plane in Figure 16(c)), respectively. The symmetric nature of these field plots is expected due to the symmetry in the pressure jumps seen earlier for this case. For a duct length of 0.5m, the solid lines in Figures 17 and 18 illustrate significant differences between the incident and scattered pressures at $\theta=90°$. These give rise to a substantial enhancement in the total field about $\theta=90°$ in the plane normal to the wide side (normal to surface $X_1=a$) of the duct. There is less apparent difference between the incident and scattered pressure in Figure 19 resulting in only a slight enhancement about $\theta=90°$ in the plane normal to the narrow side (normal to surface $X_2=b$) of the duct. Figures 17 and 19 also indicate that the monopole field is nearly unaffected by the duct in the direction of the central X_3 axis.

The enhancement seen in Figure 17 is unexpected since the results for the circular ducted fan problem presented in refs. [2-4] usually depicted shielding rather than enhancement about $\theta=90°$. However, the propeller in free-space radiates primarily in the lateral direction so that its radiation is significantly altered by the presence of the duct. The monopole radiates in all directions including axially to the ends of the duct. This difference in source type could explain the enhancement shown in Figures 17-19. In Ref. [6], the radiated field from a monopole in a circular duct was discussed. The code utilized to obtain those results was modified as discussed in Chapter 3 and an identical source to that utilized in obtaining the results for Figures 17-19 was specified. Figure 20 illustrates the directivity pattern for the scattered and total pressure fields for the circular duct at M=0. It depicts a small enhancement in the total pressure field about $\theta=90°$ for a duct length of 0.5m, and indicates that lateral shielding is obtained only if the duct length is increased to 1m or more. Thus, monopole radiation from a circular duct can also give an enhancement like that shown in Figure 17. Furthermore, it appears that the potential for shielding by the rectangular duct does exist but that the duct length needs to be increased.

The broken lines in Figures 17, 18 and 19 illustrate the effect on the scattered and total pressure directivities of increasing the rectangular duct length to 1m and 2m. As the duct length is increased, there is less apparent difference between the incident and scattered fields which indicates that the potential exists for phase cancellation in the total field. It is seen that some shielding is now obtained over the range $30°<\theta<150°$. Shielding is observed in the total pressure mainly in the center plane $X_1=0$ (normal to

narrow side) in Figure 19 and little shielding is observed in the center plane X_2=0 (normal to wide side) in Figure 17. It also appears that shielding exists only for a duct length of 2m or more. This is not surprising since the center plane normal to the narrow side exhibits less enhancement in the 0.5m case. It might be expected intuitively that the wide side of the duct should provide greater shielding from the source. However, this example shows this not to be true in general. In fact, experience indicates that few general statements can be made about the radiation patterns from ducts at low to moderate frequencies. Figures 17 and 19 also show that the duct has little apparent effect in the more nearly axial directions in the regions $150°<\theta<180°$ and $0°<\theta<30°$.

Figures 21 and 22 depict the radiated field plots for various axial and lateral cross-sectional planes for the moving duct problem as discussed in Chapter 3. The axial center planes of Figure 21 (planes in Figures 16(a) and (c)) and lateral center plane X_3=0 of Figure 22 (plane in Figure 16(b)) intersect the source. Some shielding is obtained in these planes in the total pressure about θ=90°. The moving duct does not appear to have as pronounced a channeling effect on the total radiated field as was the case for the circular duct propfan model in refs. [2-4]. This is due to the difference in source type. However, Figure 21 depicts two distinct bulges that display the impact of the singularity of the pressure jump on the leading edge and satisfaction of the Kutta condition at the trailing edge of the duct when $M \neq 0$. These are no doubt counterparts of the channeling effect seen for the propfan, but they only exist here in the plane normal to the narrow side of the duct. The figure also shows that the level of shielding provided by the wide and narrow sides of the duct does not differ as much in the presence of flow as compared to

the differences witnessed in the M=0 case in Figures 17 and 19. Because of the singularity at the leading edge of the moving duct, it is of interest to examine the directivity in the plane that contains the leading edge (X_3=-L/2). This plane is shown in Figure 16(d). The directivity in the plane containing the leading edge along with the corresponding plane containing the trailing edge (X_3=L/2) is shown in Figure 22. The incident field shown in Figure 22 is that for the X_3=0 plane since the incident fields for the leading edge, trailing edge and lateral center planes differ only slightly at M=0.1. For a duct moving in the negative X_3-direction, there appears to be greater lateral shielding at the trailing edge than at the leading edge plane, but in general there are not many differences in the radiation patterns in these planes.

Finally, to include a case more nearly representative of practical inlet experiments, the frequency is increased to 1922 Hz. At this frequency, the incident field is highly oscillatory, and a significant number of shape functions is required from the expansions (2.27) to model this field accurately (at least K_1=20, K_2=10, J=12 as a minimum). Limitations on time and computational resources lead to the decision to reduce the dimensions of the duct and thereby reduce the number of functions required to accurately model the field. The dimensions a and b were reduced by a factor of 4 (a=0.0625m, b=0.125m, L=0.5m) and only the stationary case M=0 was considered. This allowed for accurate results to be obtained with K_1=8, K_2=6 and J=12. Figure 23 (planes in Figures 16(a) and (c)) predicts significant shielding in the axial center plane normal to the wide side of the duct as would be expected because the effect of the duct at high frequencies is generally to beam sound in the axial directions. It is also of interest that, despite the relatively high frequency, virtually no shielding is provided by the narrow

side of the duct, so that the beaming effect occurs here only in planes normal to the wide side. Note that the beaming occurs even though the duct is of very short length. In the lateral planes, there is significant shielding in the region from $120°<\theta<60°$ as shown in Figure 24 (planes in Figures 16(b) and (d)). Thus the beaming seen in the plane $X_2=0$ in Figure 23 extends over a rather large angle range in the directions above the wide side of the duct.

5. Concluding Remarks

This thesis has detailed the analysis necessary to model the radiated field generated by a monopole source placed at the center of a moving rectangular duct utilizing a boundary integral technique. The total pressure in the acoustic field was written in terms of incident and scattered pressure components such that the scattered pressure represents modifications to the incident pressure due to the presence of the duct. The scattered pressure is discontinuous across the duct walls. It satisfies a generalized wave equation with a source term involving the unknown pressure jump across the duct walls. Through the use of an integral representation for the scattered pressure, a singular boundary integral equation governing the unknown jump in scattered pressure is derived. The jump is represented by a double series of carefully chosen shape functions, and a solution to the integral equation is obtained using the method of collocation. With the jumps determined, their substitution back into the integral representation of the pressure produces the radiated pressure at any observer location.

The governing equations for the analysis presented in Chapter 2 were programmed in a FORTRAN code which was run on a 500MHz DEC-Alpha workstation. The singular analysis presented in Chapter 2 isolated the effect of the singularity in the set of boundary integral equation thus eliminating problems with the implementation of numerical schemes. Numerical verification of the FORTRAN code was presented in Chapter 3. The chosen sets of shape functions were discussed and it was shown that these functions allowed for a complete analytical evaluation of the singular part of the

boundary integral equation. All the necessary numerical integrations were completed on non-singular integrals.

Radiated field results for the some problems of interest were presented in Chapter 4. For a stationary duct at a frequency of 750Hz, lateral shielding was obtained for a duct of sufficient length and was predominantly in the plane normal to the narrow side of the duct. In fact, very little shielding was obtained in the plane normal to the wide side of the duct, a result which is perhaps not expected intuitively. However, for a higher frequency case of 1922Hz, significant shielding by the stationary duct was obtained in the plane normal to the wide side of the duct. Interestingly enough, no shielding was provided by the narrow side of the duct at this relatively high frequency.

For a moving duct, the radiated field for the monopole source can be compared to that of the propeller source. The channeling effect witnessed with the moving ducted propfan was not immediately apparent in the moving ducted monopole case except for the appearance of two distinct bulges in the radiated field in the plane normal to the narrow side of the duct. At a frequency of 750Hz, comparable shielding was provided by all sides of the moving duct.

Because the analysis required to determine radiation from a rectangular duct is fully two-dimensional, it requires significantly greater computational resources than for the circular duct. Time and computer resources have allowed for only a few representative examples to be studied in this thesis. They almost certainly do not fully depict all of the interesting phenomena associated with radiation from a rectangular duct. A true understanding of the radiated field would require a detailed parametric study involving variations in duct dimensions, frequency and Mach number and it would be

beneficial to complete such a study. Furthermore, it would be a logical further step to include an acoustic liner in the rectangular duct. Unfortunately, computational requirements for this problem would greatly exceed those for the rigid walled duct.

References

1. Eversman, W., "Radiated Noise of Ducted Fans," AIAA Paper 92-02-139, 14th Aeroacoustics Conference, Aachen, May 11-14, 1992.

2. Lan, J.H., "Acoustic Shielding from a Short Rigid Duct Around a Propeller," M.S. Thesis, The George Washington University, August, 1993.

3. Buhler, J.K., "A New Boundary Integral Method for Predicting the Acoustic Field Generated by Ducted Rotating Sources," M.S. Thesis, The George Washington University, August, 1994.

4. Kosanchick, M., "The Acoustic Field Radiated by a Propeller in a Lined Duct," M.S. Thesis, The George Washington University, August, 1996.

5. Dunn, M.H., Tweed, J., Farassat, F., "The Prediction of Ducted Fan Engine Noise Via a Boundary Integral Equation Technique," AIAA-96-1770, 2nd AIAA/CEAS Aeroacoustics Conference, State College, May 6-8, 1996.

6. Myers, M. K., "Radiation of Sound From a Point Source In a Short Duct," NASA Conference Publication 3352, Second Aeroacoustics Workshop on Benchmark Problems, Tallahassee, November 4-5, 1996.

7. Özyörük , Y. and Long, L., " Solution of Aeroacoustic Problems by a Nonlinear Hybrid Method," NASA Conference Publication 3352, Second Aeroacoustics Workshop on Benchmark Problems, Tallahassee, November 4-5, 1996.

8. Farassat, F. and Myers, M. K., "Aerodynamics via Acoustics: Application of Acoustic Formulas for Aerodynamic Calculations," AIAA Paper 86-1877, 10th Aeroacoustics Conference, Seattle, July 9-11, 1986.

9. Farassat, F., "Introduction to Generalized Functions with Applications in Aerodynamics and Aeroacoustics," NASA Technical Paper 3428, Langley Research Center, Hampton, May, 1994 (corrected April 1996).

10. Morse, Philip M. and Ingard, K. Uno, Theoretical Acoustics, McGraw-Hill, Inc., New York, 1968.

11. Karamcheti, K., Principles of Ideal-Fluid Aerodynamics, Kreiger Publishing Company, Inc., Malabar, Fl, 1980.

12. Reddy, J.N., An Introduction to the Finite Element Method, 2nd Edition, McGraw-Hill, Inc., New York, 1993.

13. Burden, R.L. and Faires, J.D., Numerical Analysis, 5th Edition, PWS-KENT Publishing Company, Boston, 1993.

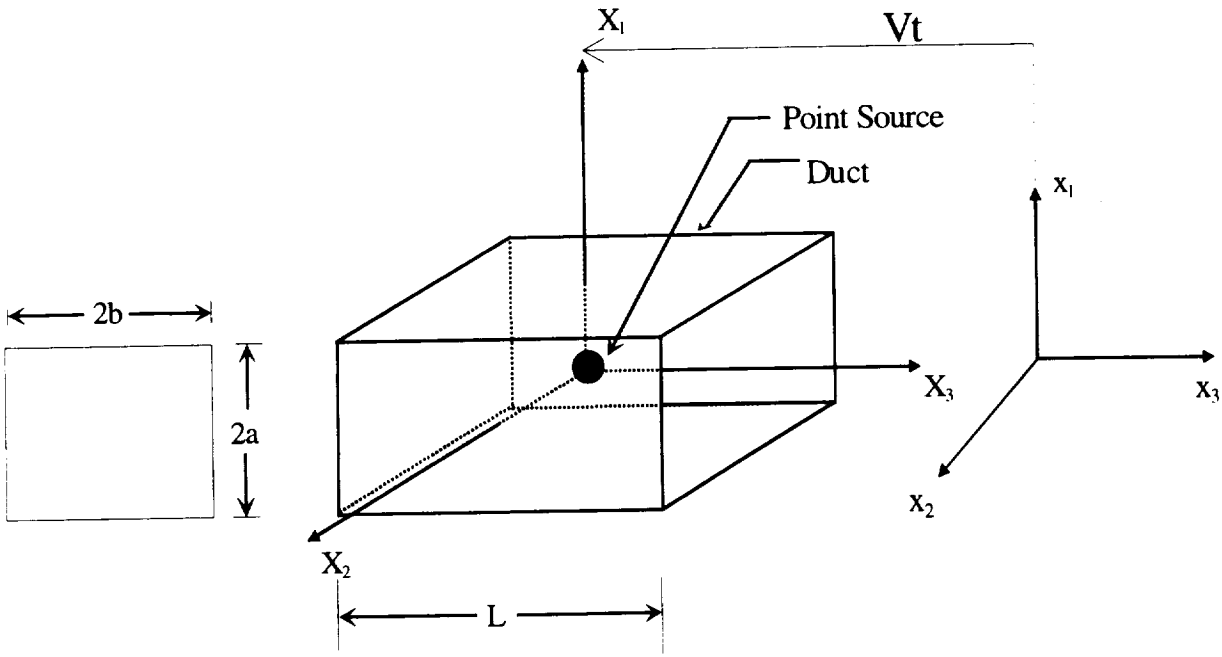

Figure 1: Geometry and Coordinate Systems

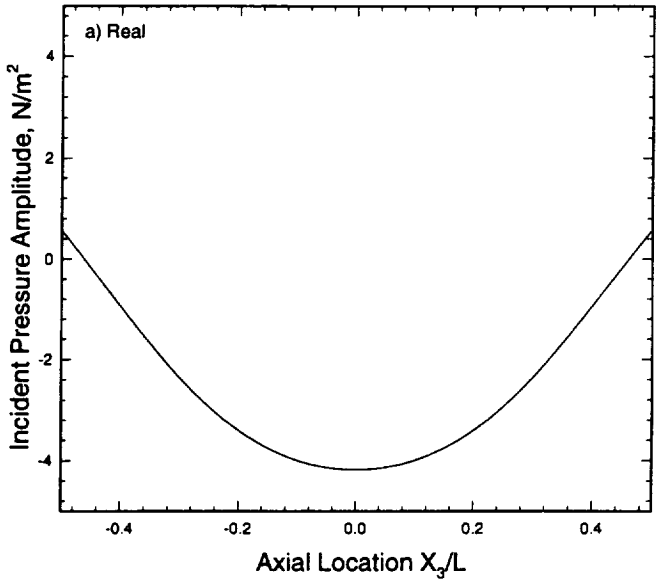

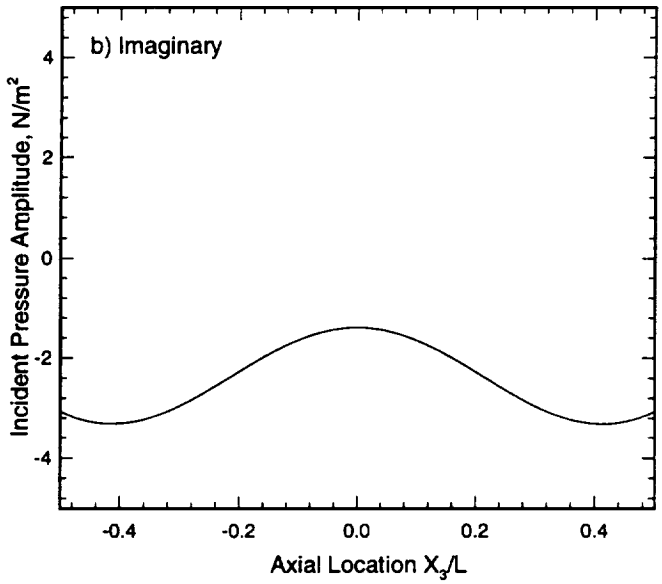

Figure 2: Incident Pressure Amplitude in plane X_2=0 on Duct Surface X_1=a; a=0.25m, b=0.5m, L=0.5m, f=750Hz, M=0.0

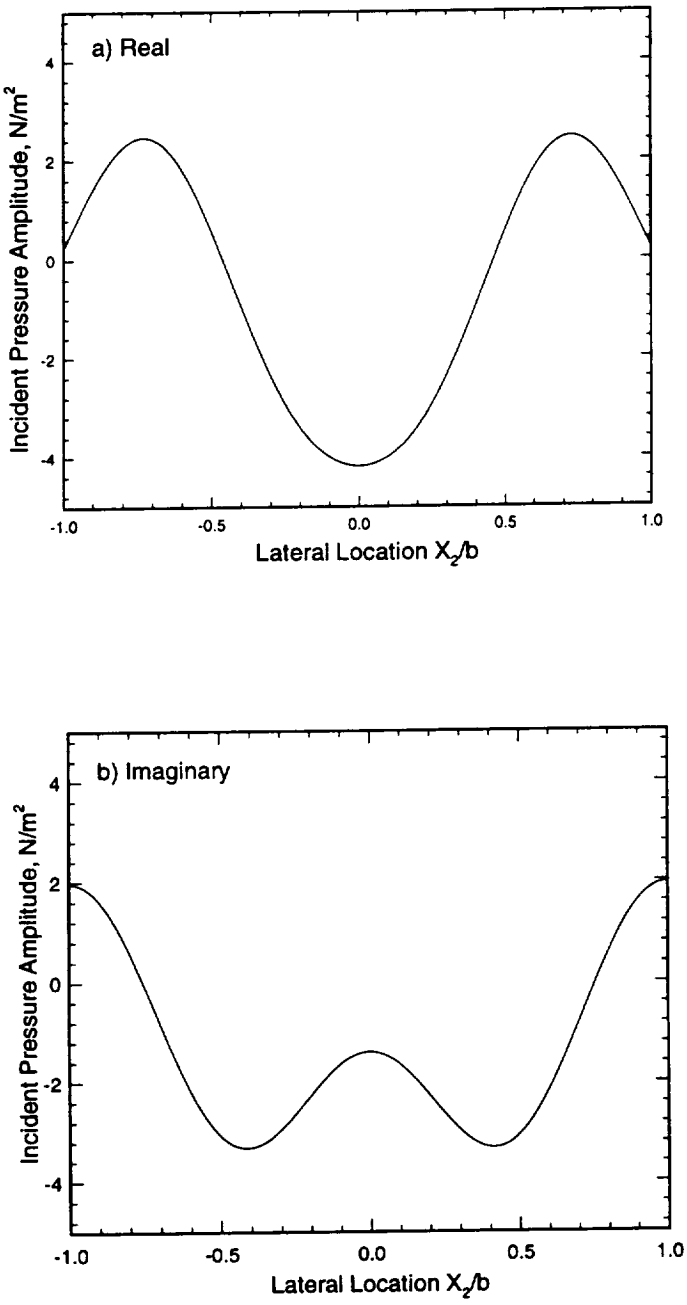

Figure 3: Incident Pressure Amplitude in plane X_3=0 on Duct Surface X_1=a; a=0.25m b=0.5m, L=0.5m, f=750Hz, M=0.0

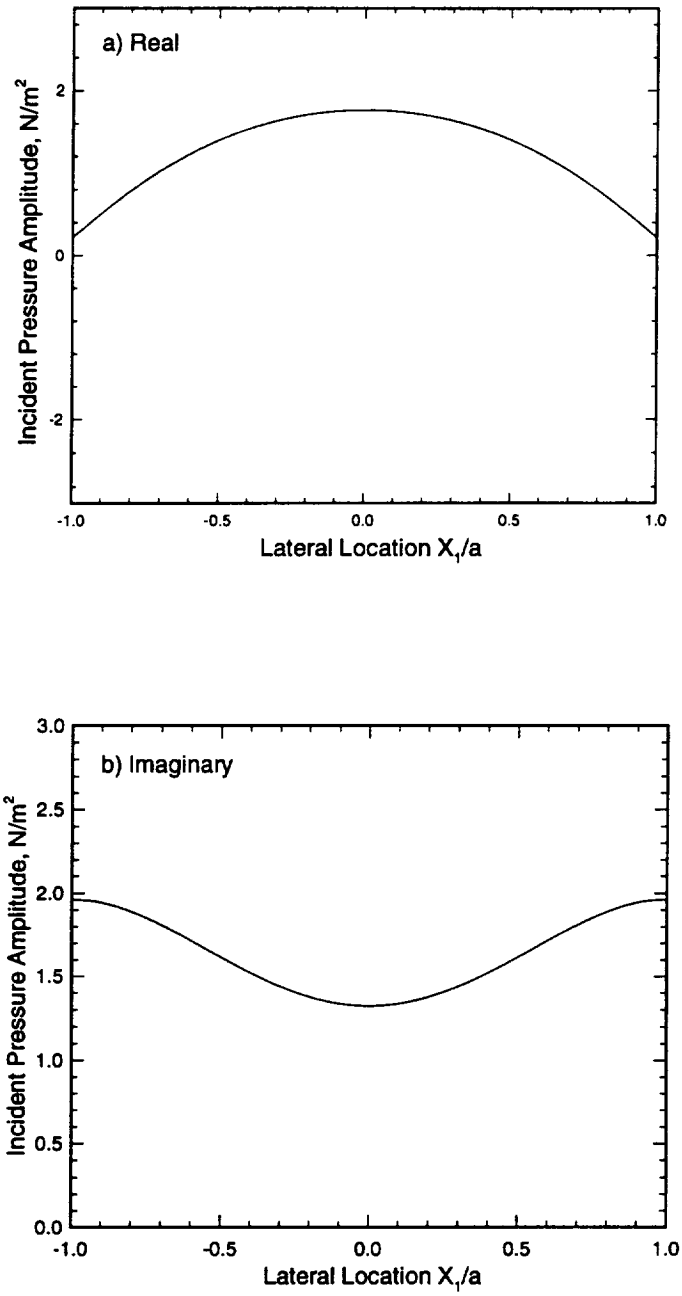

Figure 4: Incident Pressure Amplitude in plane X_3=0 on Duct Surface X_2=b; a=0.25m b=0.5m, L=0.5m, f=750Hz, m=0.0

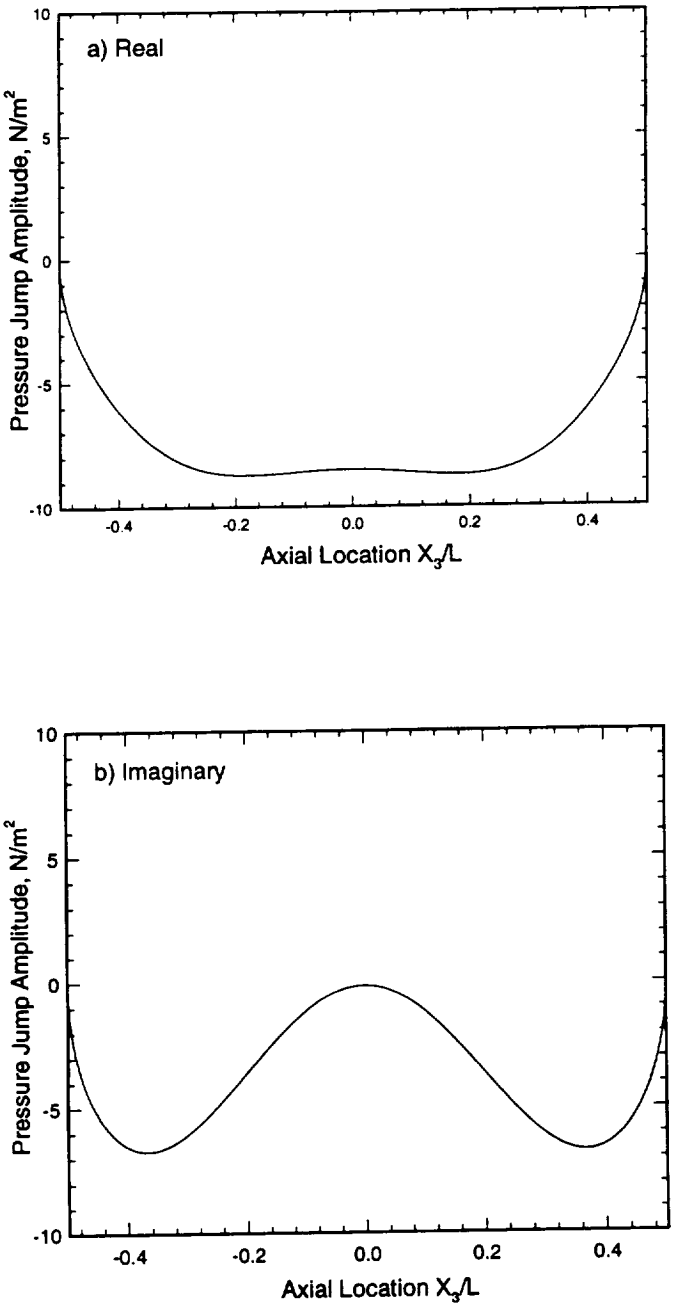

Figure 5: Scattered Pressure Jump Amplitude in plane X_2=0 on Duct Surface X_1=a; a=0.25m b=0.5m, L=0.5m, f=750Hz, M=0.0

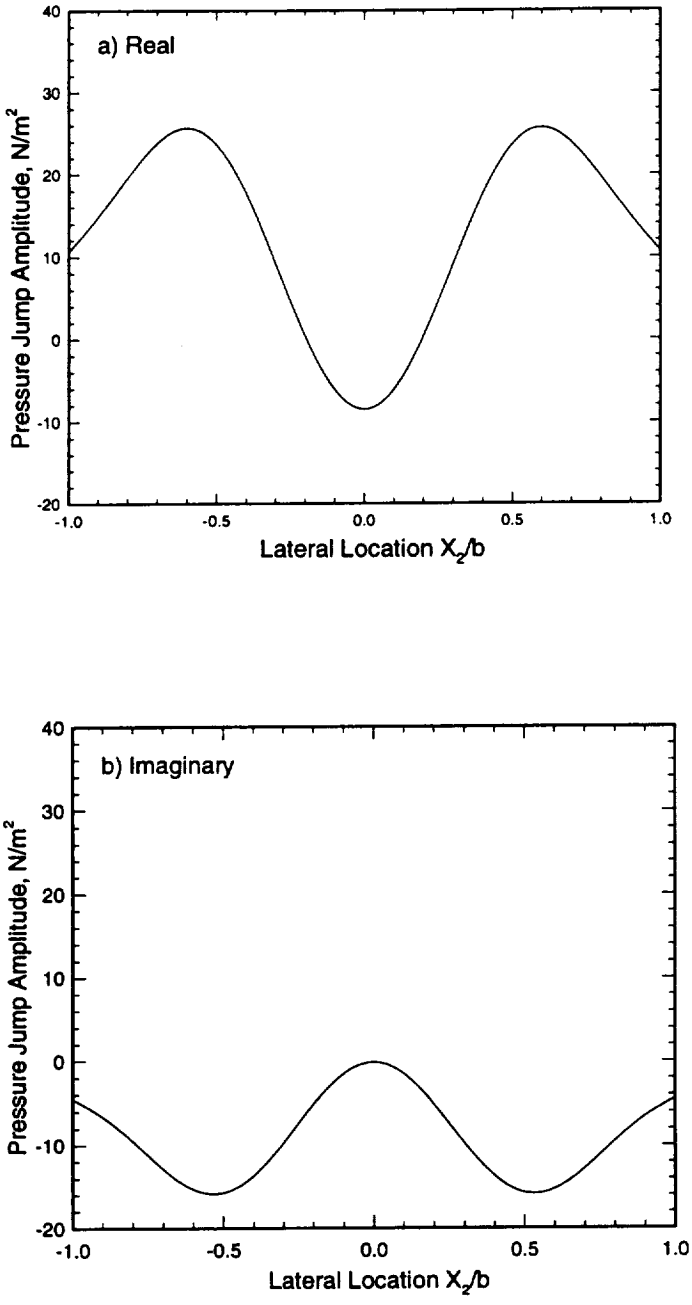

Figure 6: Scattered Pressure Jump Amplitude in plane X_3=0 on Duct Surface X_1=a; a=0.25m b=0.5m, L=0.5m, f=750Hz, M=0.0

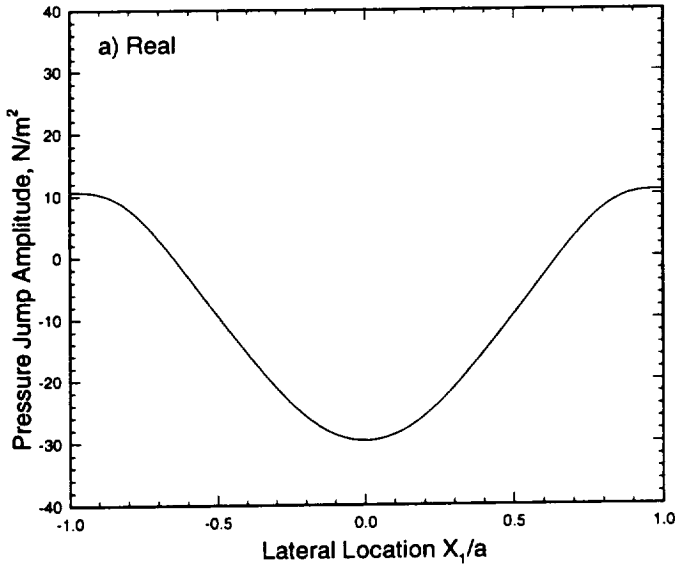

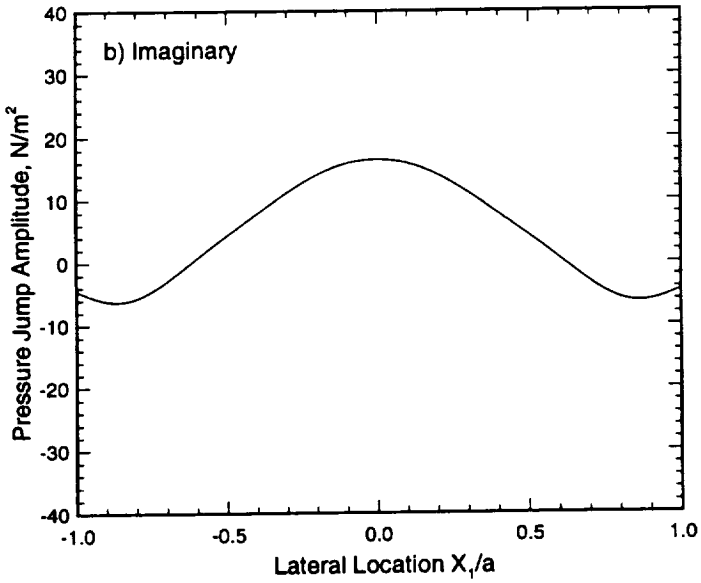

Figure 7: Scattered Pressure Jump Amplitude in plane X_3=0 on Duct Surface X_2=b; a=0.25m, b=0.5m, L=0.5m, f=750Hz, M=0.0

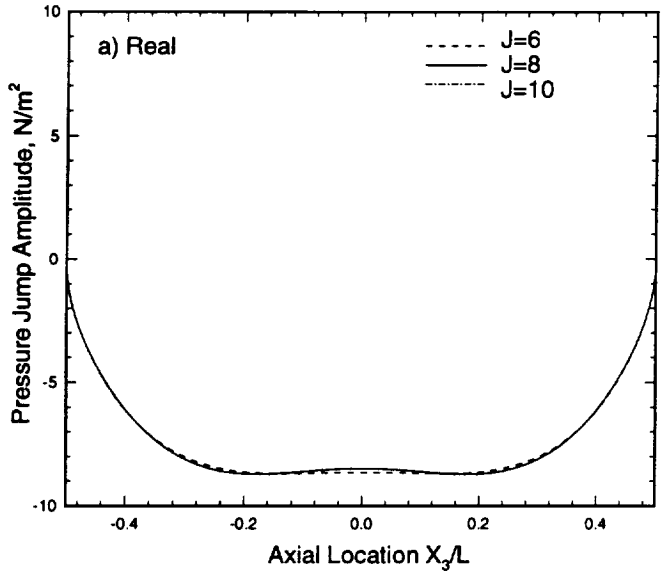

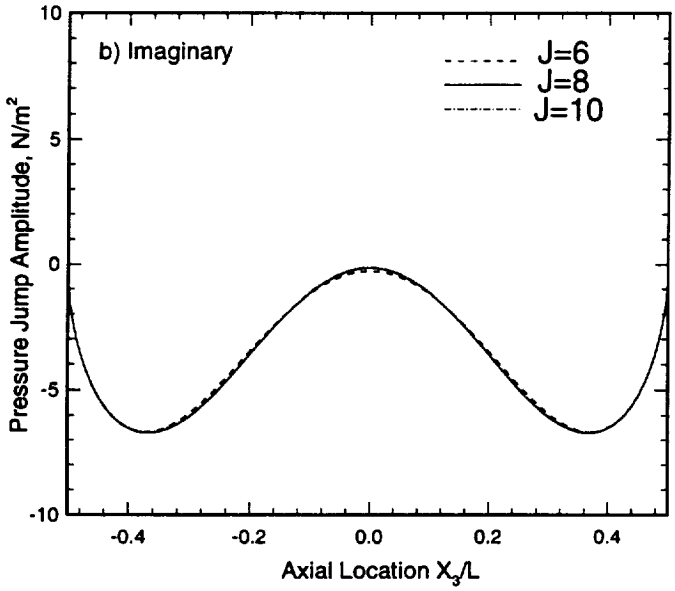

Figure 8: Scattered Pressure Jump Amplitude in plane X_2=0 on Duct Surface X_1=a; a=0.25m b=0.5m, L=0.5m, f=750Hz, M=0.0, K_1=8, K_2=6

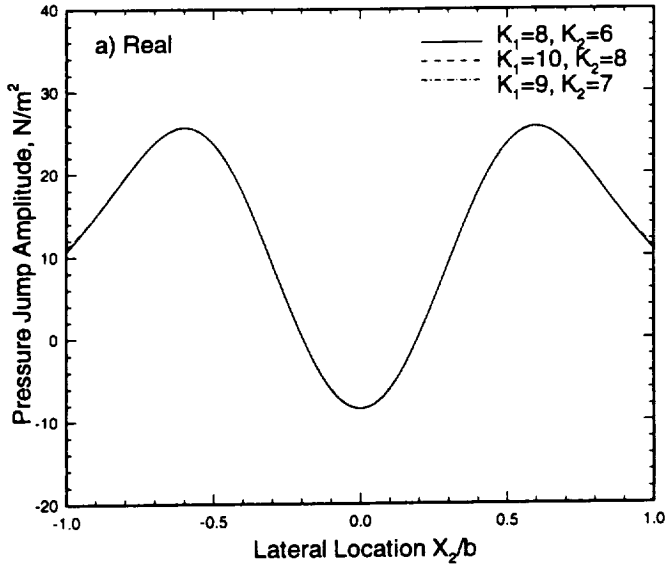

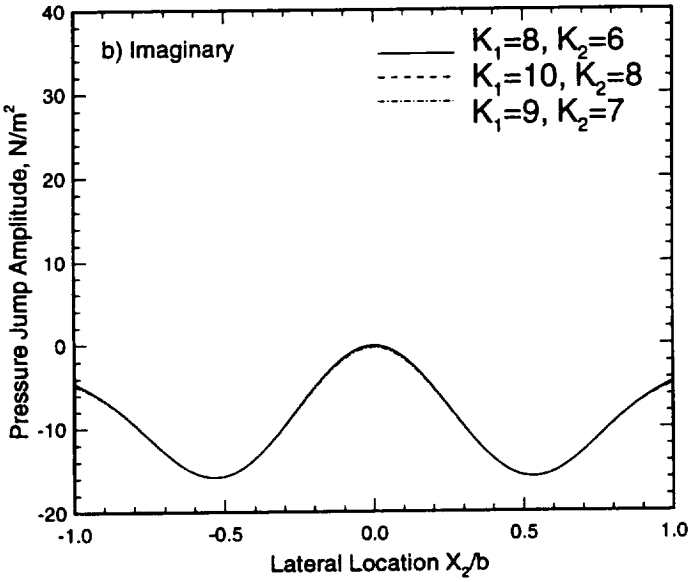

Figure 9: Scattered Pressure Jump Amplitude in plane X_3=0 on Duct Surface X_1=a; a=0.25m b=0.5m, L=0.5m, f=750Hz, M=0.0, J=8

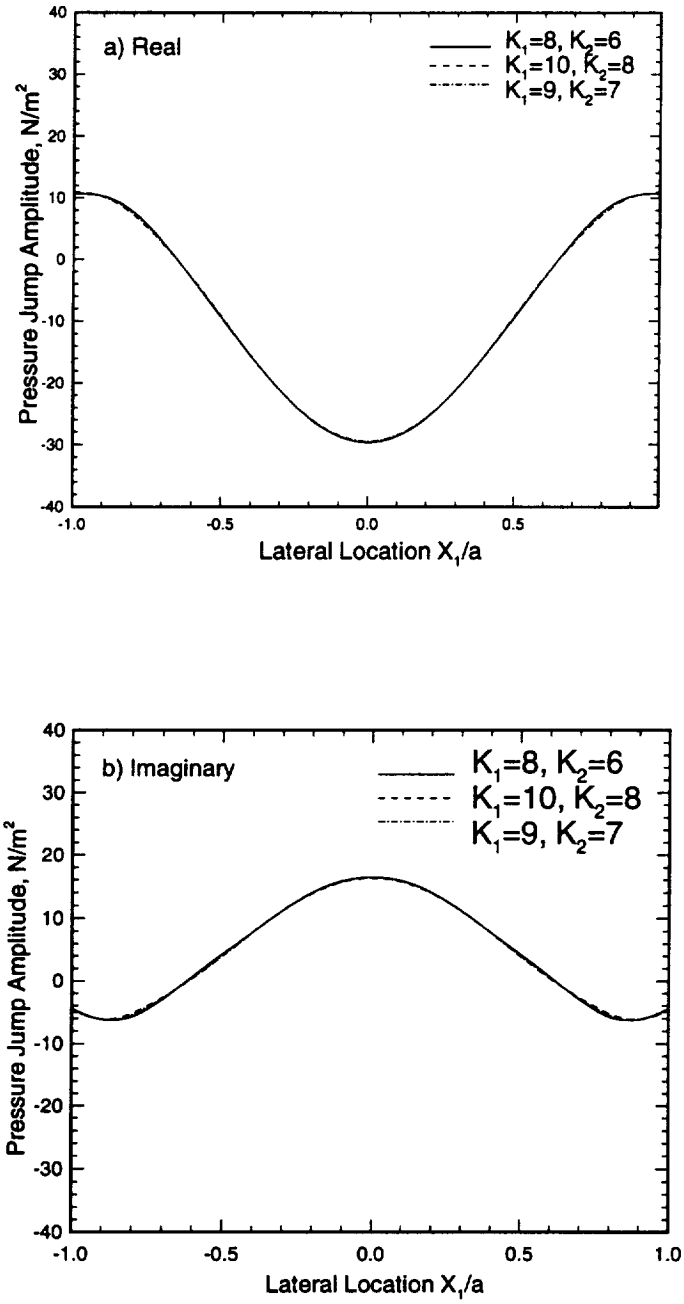

Figure 10: Scattered Pressure Jump Amplitude in plane X_3=0 on Duct Surface X_2=b; a=0.25m b=0.5m, L=0.5m, f=750Hz, M=0.0, J=8

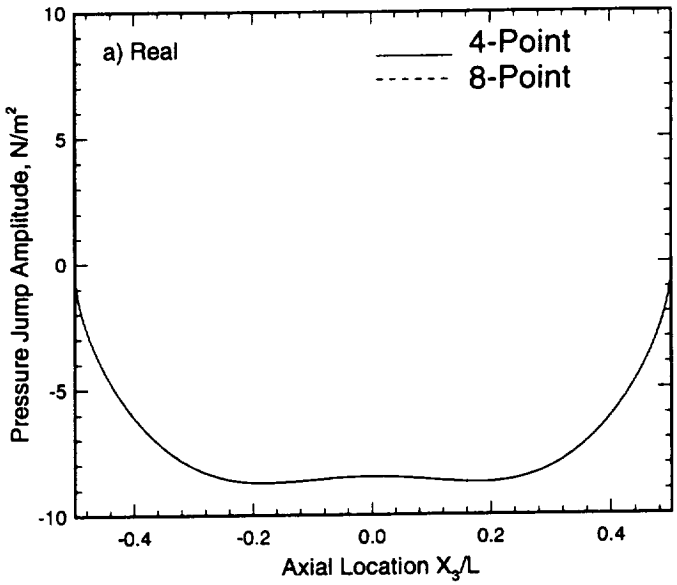

Figure 11: Real Part of Scattered Pressure Jump Amplitude in plane X_2=0 on Duct Surface X_1=a using Different Order Gauss-Legendre Schemes a=0.25m, b=0.5m, L=0.5m, f=750Hz, M=0.0

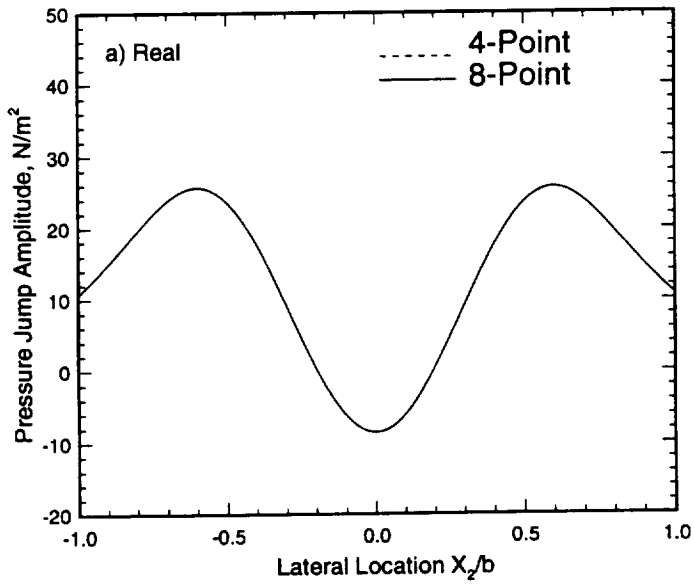

Figure 12: Real Part of Scattered Pressure Jump Amplitude in plane X_3=0 on Duct Surface X_1=a using Different Order Gauss-Legendre Schemes a=0.25m, b=0.5m, L=0.5m, f=750Hz, M=0.0

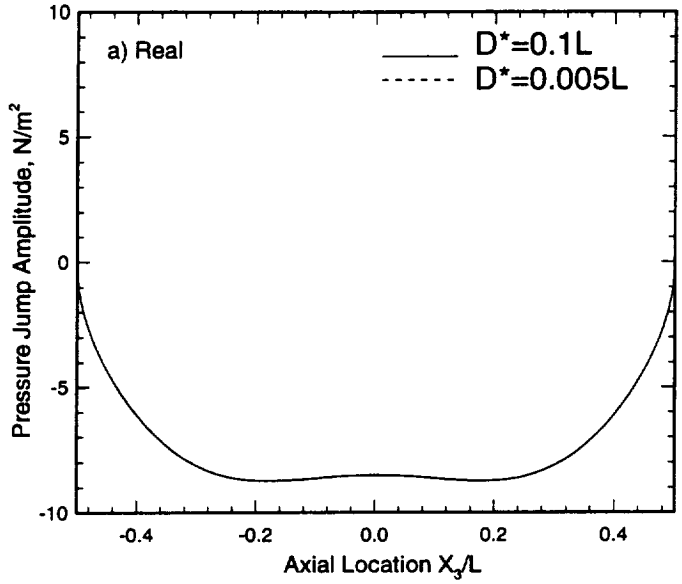

Figure 13: Real Part of Scattered Pressure Jump Amplitude in plane X_2=0 on Duct Surface X_1=a with Different Sets of Collocation Points; a=0.25m, b=0.5m, L=0.5m, f=750Hz, M=0.0

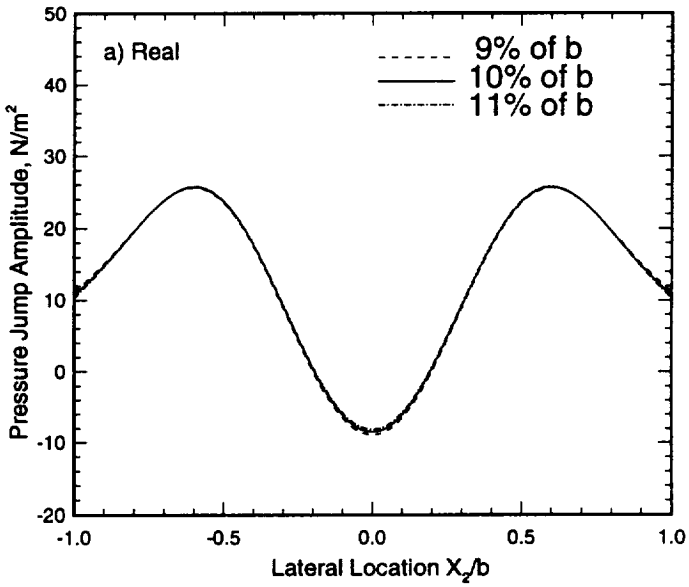

Figure 14: Real Part of Scattered Pressure Jump Amplitude in plane X_3=0 on Duct Surface X_1=a with Different Sets of Collocation Points; a=0.25m, b=0.5m, L=0.5m, f=750Hz, M=0.0

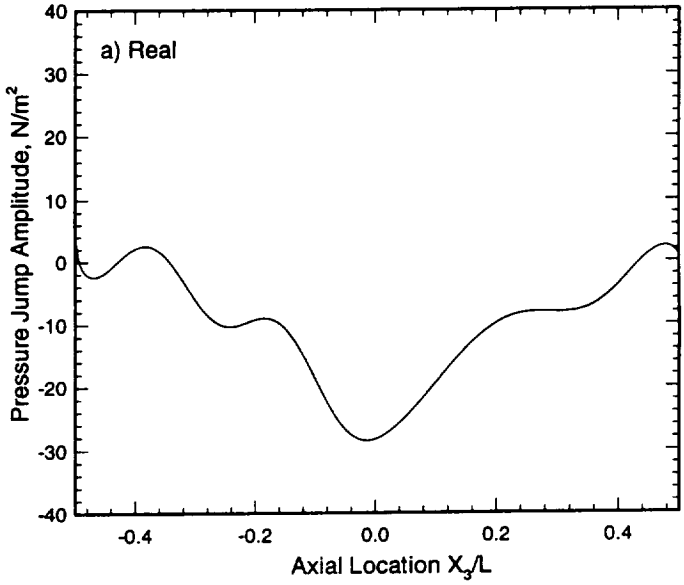

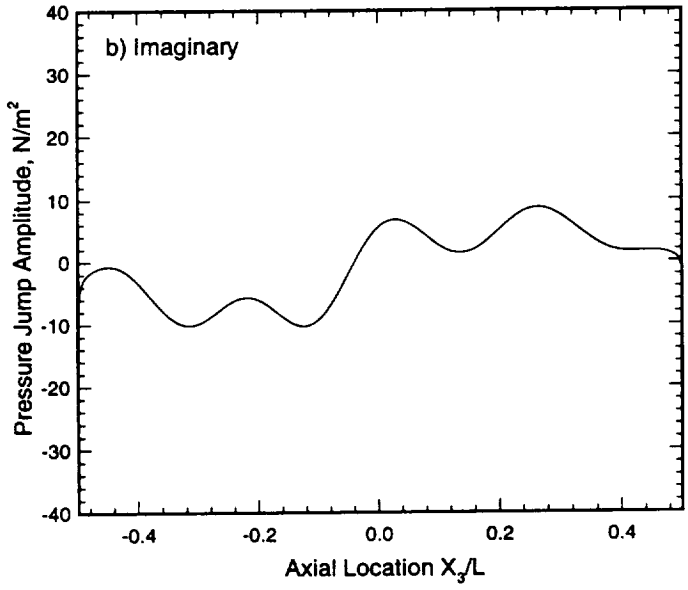

Figure 15: Scattered Pressure Jump Amplitude in plane X_2=0 on Duct Surface X_1=a; a=0.25m, b=0.5m, L=2.0m, f=750Hz, M=0.1

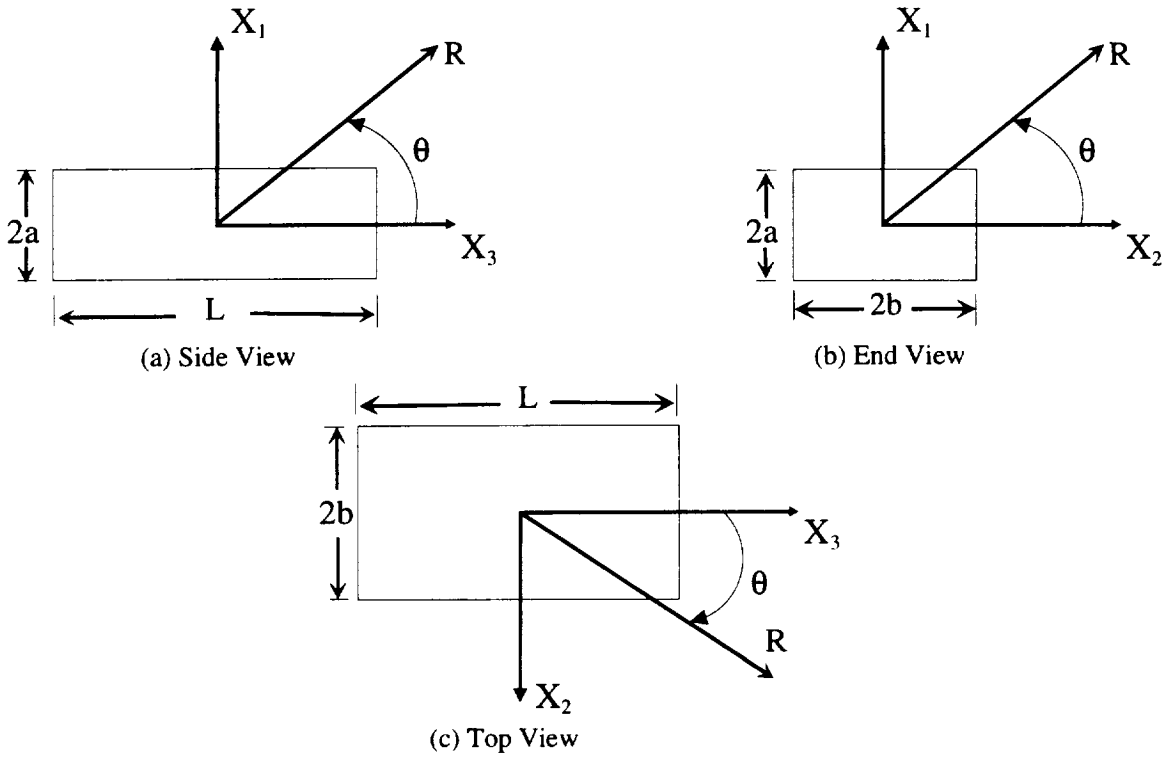

Figures 16 (a)-(c): Spherical Radius for Radiated Field

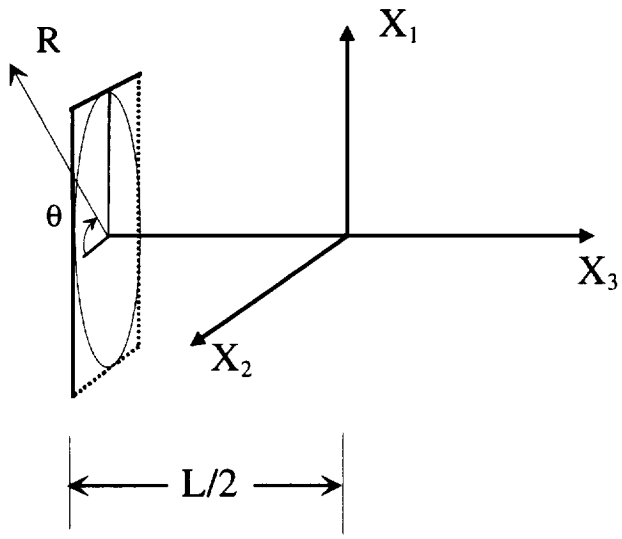

Figure 16 (d): Intersection of Plane and Sphere

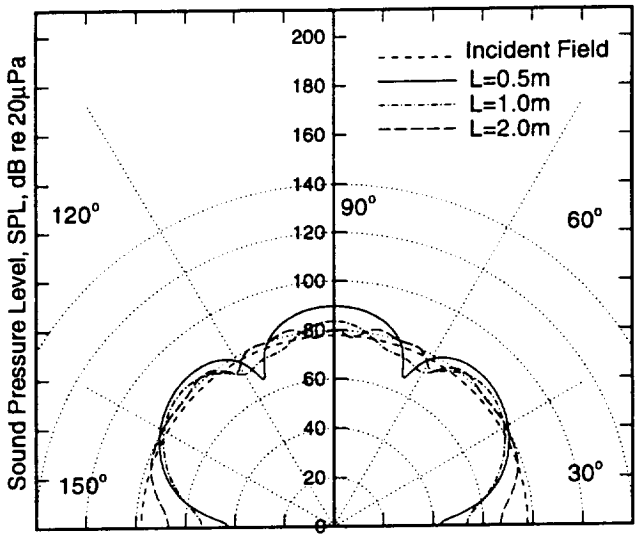

Figure 17 (a): Scattered Field in plane X_2=0 at Spherical Radius of 5m; a=0.25m, b=0.5m, f=750Hz, M=0.0

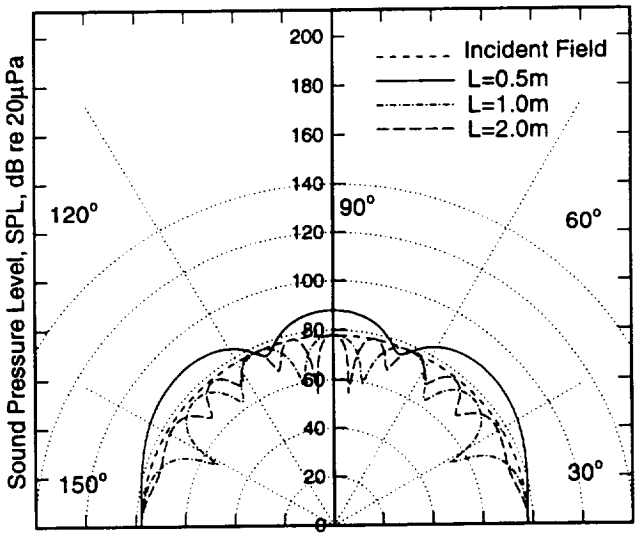

Figure 17 (b): Total Field in plane X_2=0 at Spherical Radius 5m; a=0.25m, b=0.5m, f=750Hz, M=0.0

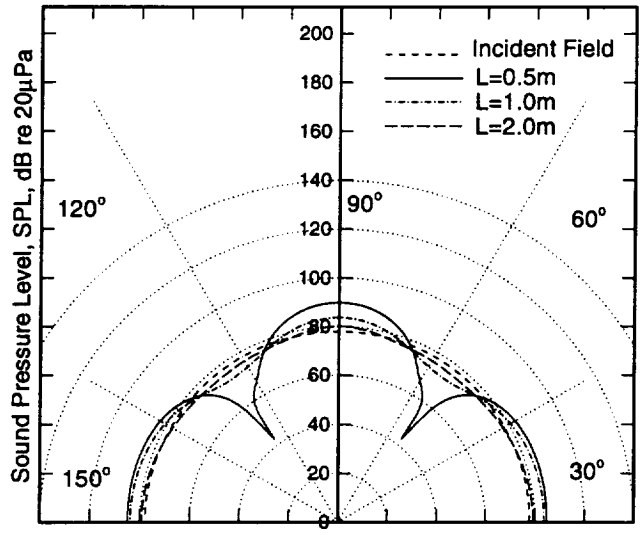

Figure 18 (a): Scattered Field in plane X_3=0 at Spherical Radius 5m; a=0.25m, b=0.5m, f=750Hz, M=0.0

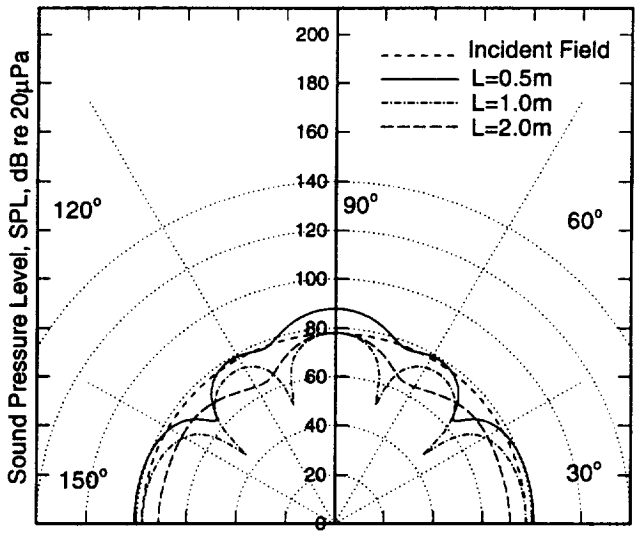

Figure 18 (b): Total Field in plane X_3=0 at Spherical Radius 5m; a=0.25m, b=0.5m, f=750Hz, M=0.0

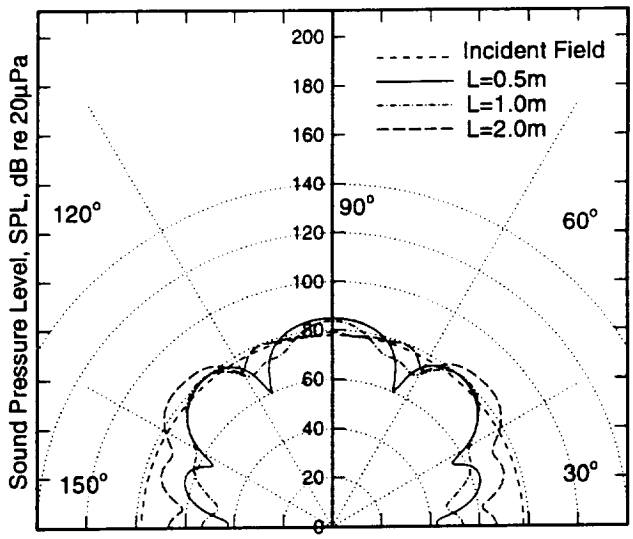

Figure 19 (a): Scattered Field in plane X_1=0 at Spherical Radius 5m; a=0.25m, b=0.5m, f=750Hz, M=0.0

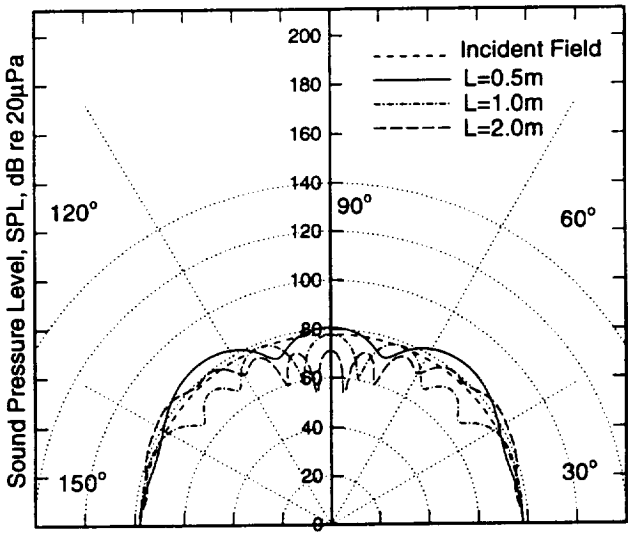

Figure 19 (b): Total Field in plane X_1=0 at Spherical Radius 5m; a=0.25m, b=0.5m, f=750Hz, M=0.0

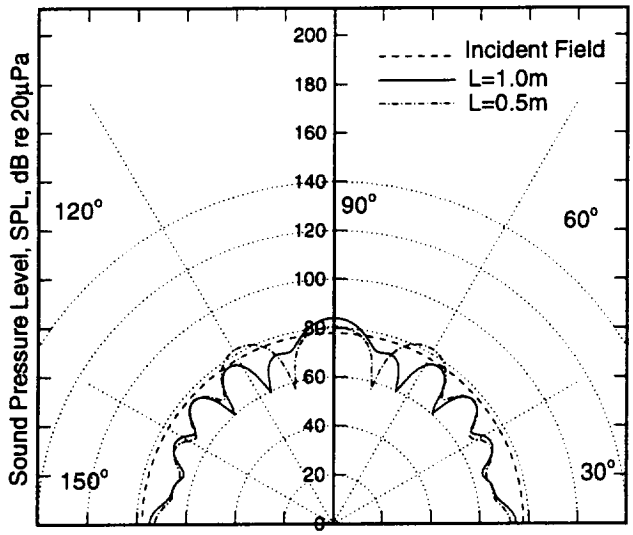

Figure 20 (a): Scattered Field in plane X_2=0 at Spherical Radius 5m; M=0.0, Circular Duct Radius=1.0m

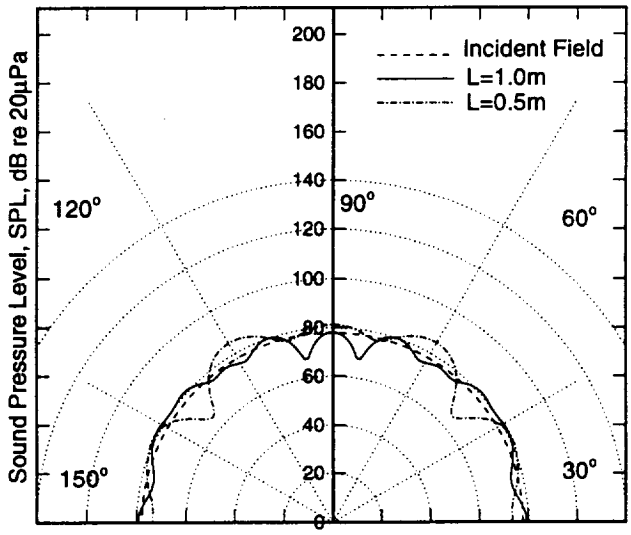

Figure 20 (b): Total Field in plane X_2=0 at Spherical Radius 5m; M=0.0, Circular Duct Radius=1.0m

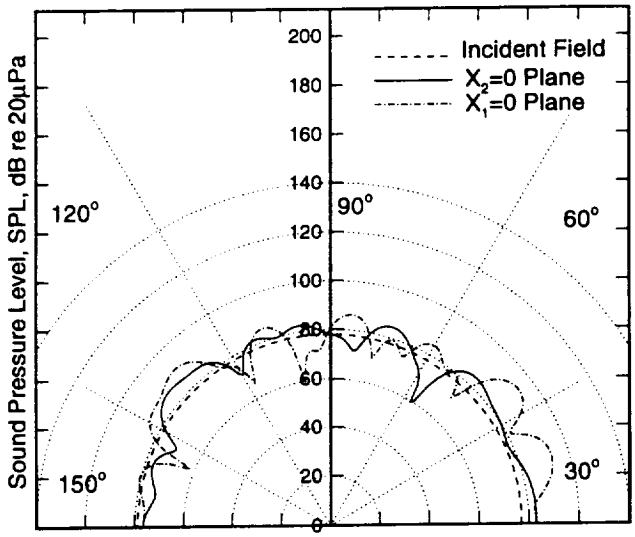

Figure 21 (a): Scattered Field at Spherical Radius 5m for Moving Duct; a=0.25m, b=0.5m, L=2.0m, f=750Hz, M=0.1

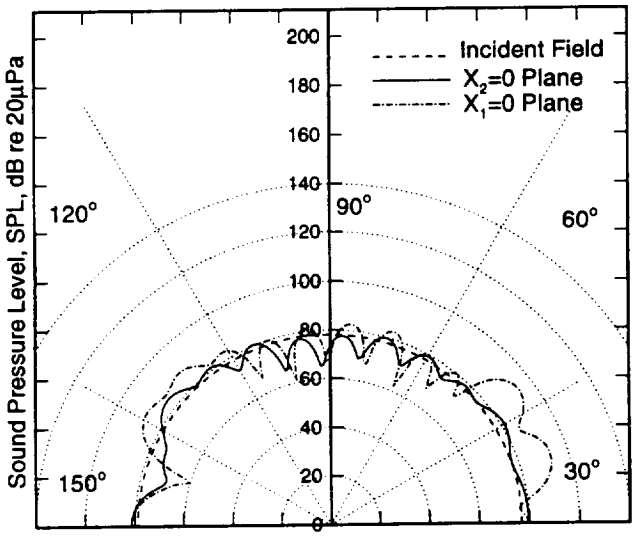

Figure 21 (b): Total Field at Spherical Radius 5m for Moving Duct; a=0.25m, b=0.5m, L=2.0m, f=750Hz, M=0.1

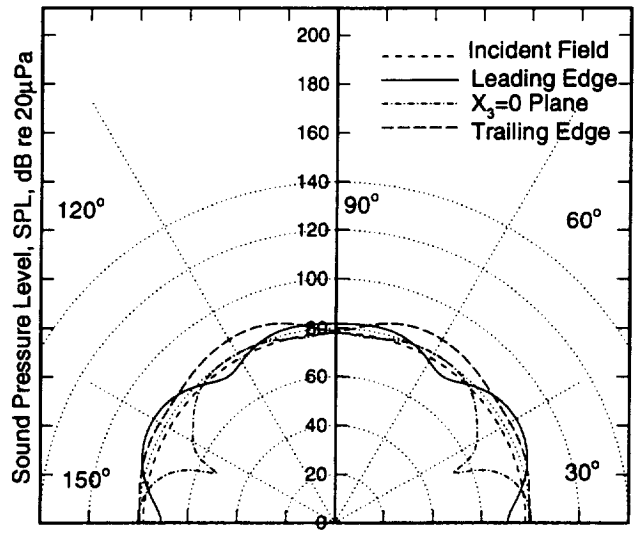

Figure 22 (a): Scattered Field at Spherical Radius 5m for Moving Duct; a=0.25m, b=0.5m, L=2.0m, f=750Hz, M=0.1

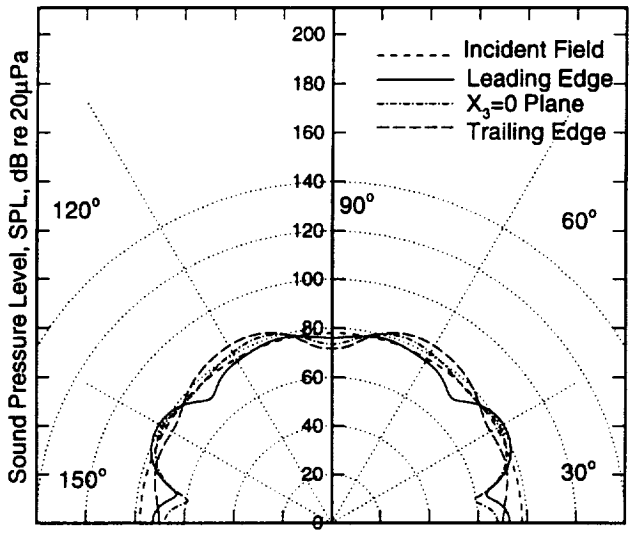

Figure 22 (b): Total Field at Spherical Radius 5m for Moving Duct; a=0.25m, b=0.5m, L=2.0m, f=750Hz, M=0.1

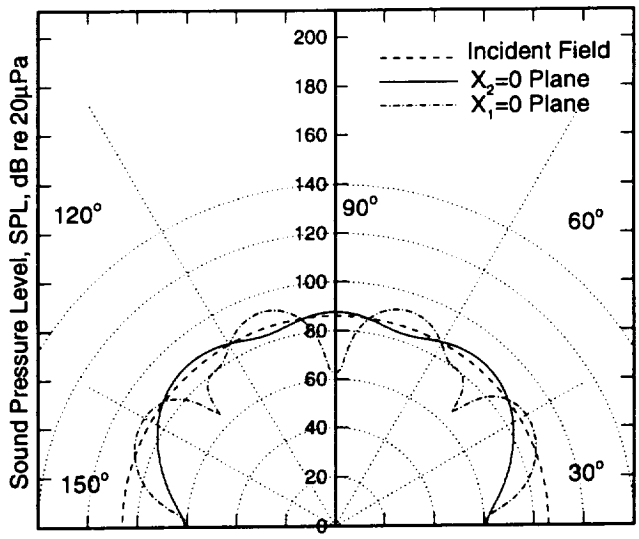

Figure 23 (a): Scattered Field at Spherical Radius 5m; a=0.0625m, b=0.125m, L=0.5m, f=1922Hz, M=0.0

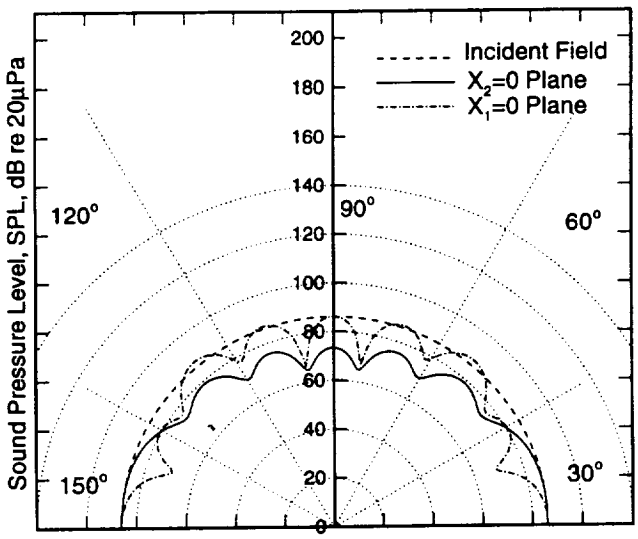

Figure 23 (b): Total Field at Spherical Radius 5m; a=0.0625m, b=0.125m, L=0.5m, f=1922Hz, M=0.0

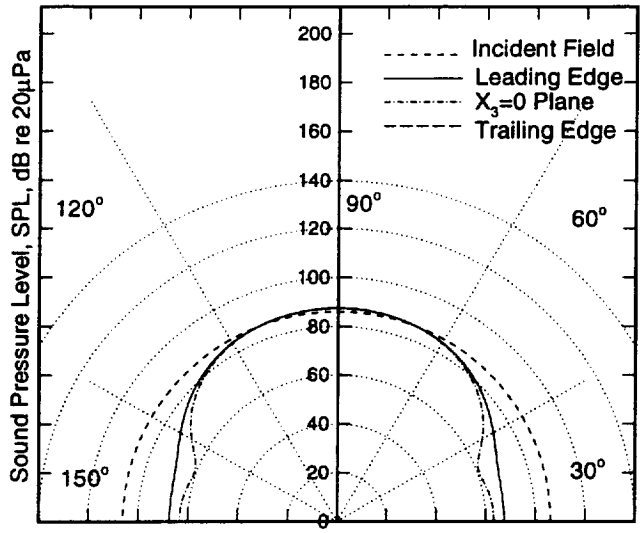

Figure 24 (a): Scattered Field at Spherical Radius 5m; a=0.0625m, b=0.125m, L=0.5m, f=1922Hz, M=0.0

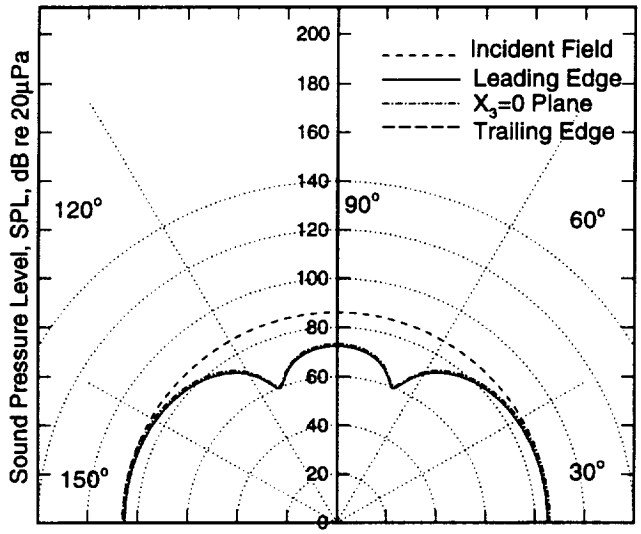

Figure 24 (b): Total Field at Spherical Radius 5m; a=0.0625m, b=0.125m L=0.5m, f=1922Hz, M=0.0